DEPARTMENT OF PHYSICS, UNIVERSITY OF JYVÄSKYLÄ
RESEARCH REPORT No. 2/2003

HIGH PERFORMANCE MICROBOLOMETERS AND MICROCALORIMETERS: FROM 300 K TO 100 mK

BY
ARTTU LUUKANEN

Academic Dissertation
for the Degree of
Doctor of Philosophy

To be presented, by the permission of the
Faculty of Mathematics and Science
of the University of Jyväskylä,
for public Examination in Auditorium FYS-1 of the
University of Jyväskylä on May 9, 2003
at 12 o'clock noon.

Jyväskylä, Finland
May 2003

ISBN 978-951-39-3140-7

URN:ISBN:978-951-39-3140-7

Abstract

This thesis is a review of six publications which focus on the development of thermal detectors and on-chip coolers. The thermal detectors developed are antenna coupled microbolometers and transition-edge microcalorimeters. The bolometers are intended for the detection of submillimetre waves, a region in the electromagnetic spectrum located between the infrared and microwave frequencies, in which detection methods are least developed. A room temperature bolometer is presented, which is suitable for applications where large levels of signal power are present, such as solar astronomy or imaging of concealed weapons under clothing when combined with an illumination source, while the sensitivity of a novel superconducting bolometer, operated at 4.2 K, is more than sufficient for passive imaging of terrestrial sources. The figure of merit for this detector is shown to be about an order of magnitude better than that of existing 4.2 K bolometers.

Results obtained with X-ray transition-edge sensor (TES) microcalorimeters, the most sensitive type of X-ray detector in terms of energy resolution to date, are presented. These devices are operated at temperatures below 100 mK, and can achieve energy resolutions of a few electron volts. The TES microcalorimeters will be used in future X-ray science missions of the European Space Agency (ESA), the U.S. National Astronautics and Space Administration (NASA), and the National Space Development Agency of Japan (NASDA). Until recently, the behaviour of these devices has been well understood, but there have been a number of reports that the performance of the detectors does not achieve that predicted by the theory. We have developed a Corbino disk geometry TES, which is used as a diagnostic tool to investigate the origins of the excess noise. We show that the excess noise can be accurately modeled with a noise arising from fluctuational superconductivity from regions of the TES which are close to the critical temperature T_c. We predict that this noise source will be of significance in TESs operated at large bias currents and low operating point resistances. Ways to decrease this noise contribution are presented.

The cooling of detectors to temperatures well below 1 K is a challenging task. As a last part of this thesis we present the results obtained with a novel type of cooler where the cooling effect is based on the evaporative cooling of electrons from a normal metal island. These devices can cool efficiently the electron gas by a factor of 3 from 0.3 K to 0.1 K. Related to this, it is shown that the cooling of the electron gas alone does not improve the sensitivity of thermal detectors sufficiently, and consequently that the cooling of the lattice is desirable. With the lattice coolers presented, cooling of an isolated silicon nitride platform from 0.2 K to 0.1 K is demonstrated. Further increase of the cooling power is possible by increasing the size of the tunnel junctions.

parallel TESs are required. Using the parameters from our CorTES data, however, we would need to have $n \sim 10^2$ parallel TESs, which renders this approach impractical.

It can be concluded that critical fluctuation effects are of fundamental nature in transition-edge sensors, and will be the limiting noise source when operated at very small bias resistances, where these sensors would otherwise exhibit optimum performance.

Preface

This work has been carried out in the Physics department of the University of Jyväskylä, Finland.

First of all, I thank my supervisor Prof. Jukka Pekola for his dedicated guidance of my work, and his ability to see through the clutter of lesser issues to the hard core of a physical problem. It has been a great pleasure to work with him. Apart from Jukka, I am deepdly indebted to a large group of people. Especially important to my career has been Dr. Heikki Sipilä, who hired me to work for Metorex already in 1994, and who I am to thank for choosing to work with thermal detectors in the first place. Moreover, the experience of working for a company has provided me with invaluable knowledge on how to conduct project oriented research.

From Jyväskylä, I thank the departmental staff, and the entire applied physics group for enjoyable comradeship, and especially Antti Nuottajärvi, whose expertise in the thin film processing combined with a resilient attitude was invaluable for this work. The other irreplaceable 'clean room wizard' is Tarmo Suppula, who produced the SINIS samples and with whom I had a number of important discussions relating to the technological challenges in sample fabrication. Also the contribution of Kimmo Kinnunen is acknowledged for helping me with the cryogenic measurements over the years, and also for many discussions.

I gratefully acknowledge the comments, ideas, assistance, hardware and insights kindly and generously supplied by Konstantin Arutyunov, Marcel Bruijn, Bernard Collaudin, Erich Grossman, Klavs Hansen, Tero Heikkilä, Panu Helistö, Juhani Huovelin, Vladimir Khaikin, Jani Kivioja, Mikko Kiviranta, Nikolai Kopnin, Piet de Korte, Martin Kulawski, Jan van der Kuur, Leonid Kuzmin, Mark Lindeman, Peter de Maagt, Ilari Maasilta, Juha Mallat, Didier Martin, Wim Mels, Seppo Nenonen, Antti Niskanen, Heikki Seppä, Jussi Tuovinen, Joel Ullom, and Seppo Vaijärvi, as well as contributions from all those I have forgotten to mention.

I had many interesting discussions with my co-authors, who I thank for delightful collaboration: Jouni Ahopelto, Dragos Anghel, Wouter Bergmann Tiest, Henk Hoevers, Mikko Leivo, Antti Manninen, Mika Prunnila, and Alexander Savin.

Financial support from the Jenny and Antti Wihuri foundation, the Academy of Finland, and the European Space Agency are kindly acknowledged.

And finally, I thank my parents, and friends for their support. My deepest gratitude is to Vilja, for putting up with me and being such a lovely companion.

Espoo, April, 2003

Arttu Luukanen

List of Publications

This thesis is a review of the author's work in the field of room temperature bolometers, cryogenic X-ray radiation detectors, and tunnel junction refrigerators. It consists of an overview and the following selection of the author's publications in the field:

I. A. Luukanen, H. Sipilä, K.M. Kinnunen, A.K. Nuottajärvi, and J.P. Pekola, *Transition-edge microcalorimeters for X-ray space applications*, Physica B **284-288**, 2133-2134 (2000).

II. A. Luukanen, M.M. Leivo, J.K. Suoknuuti, A.J. Manninen and J.P. Pekola, *On-chip refrigeration of hot electrons at sub-kelvin temperatures*, J. Low Temp. Phys. **120**, 281–290 (2000).

III. D.V. Anghel, A. Luukanen, and J.P. Pekola, *Performance of cryogenic microbolometers and microcalorimeters with on-chip coolers*, Appl. Phys. Lett. **78**, 556–558 (2001).

IV. A. Luukanen, A.M. Savin, T.I. Suppula, J.P. Pekola, M. Prunnila, and J. Ahopelto, *Integrated SINIS refrigerators for efficient cooling of cryogenic detectors*, in LTD-9 AIP Conference Proceedings **605**, 375–378 (2002).

V. A. Luukanen and J.P. Pekola, *A superconducting antenna-coupled hot-spot microbolometer*, to appear in Appl. Phys. Lett. **82**, (2003).

VI. A. Luukanen, K.M. Kinnunen, A.K. Nuottajärvi, H.F.C. Hoevers, W.M. Bergmann Tiest, and J.P. Pekola, *Fluctuation superconductivity limited noise in a transition-edge sensor*, accepted for publication in Phys. Rev. Lett. (2003).

Author's Contribution

The research reported in this thesis was carried out at the Physics Department of University of Jyväskylä during the years 1998-2003. The author has written papers I, V and VI, and participated in writing papers II, III and IV. In paper III, the author contributed to the theoretical analysis. The author carried out a significant proportion of the sample fabrication, measurements, and data analysis in papers I and VI, and participated in the measurements and data analysis in papers II and IV. In paper V, the author carried out all of the sample fabrication and measurements, and performed most of the data analysis.

Contents

1 Introduction

1.1 The electromagnetic spectrum

Electromagnetic radiation envelopes us humans here on Earth, and in fact perpetrates the entire Universe. All bodies emit a specific type of radiation whose spectrum, or colour, is determined by the physical temperature of the object. This radiation is commonly known as *blackbody radiation*. Our vision is based on the interaction of radiation with a complex sensory system, the eye and the cortex in our brain. Due to the physical characteristics of the central star in our solar system, the Sun, most of the living entities on earth detect electromagnetic radiation in a fairly narrow wavelength range, which is commonly known as visible light. Determined by its surface temperature, the Sun emits most of its energy in this wavelength range, and thus evolution, as it tends to favour efficiency, has provided us with sensors specialized to visible light as there is an abundance of signal available. By no means is the visible region the only interesting region in the electromagnetic spectrum. The spectrum, shown in Fig. 1, can be divided to subdivisions with familiar names. Starting from long wavelengths, radio waves span the region down to a wavelength of one centimeter, where the microwave region starts. Microwaves correspond to wavelengths between 10 cm down to about 1 cm. Reducing the wavelength to a millimeter, the region is quite naturally called the millimeter wave region, which continues to the submillimeter wave region down to a wavelength of about 100 micrometers (one micrometer corresponds to one thousandth of a millimeter). These regions are of relevance to this research and will be looked upon in more detail later. The region between 100 micrometers and 1 micrometer is the infrared region, for which the evolution has kindly provided a sensor - the skin. Most of us will find it difficult to roast a sausage in a large campfire if equipped with too short of a stick: a burning sensation on your skin is due to the infrared radiation, most of which is emitted at a wavelength λ given by Wien's displacement law: $\lambda = 2.898 \times 10^{-3}\mathrm{K\ m}/T_{\mathrm{campfire}} = 2.2\ \mu\mathrm{m}$. After the visible and ultraviolet wavelengths, the radiation is commonly known as X-rays, a penetrating type of radiation which also possesses some danger to living organisms due to its ionizing nature. The sun is also a strong emitter of X-rays, but these are fortunately blocked by the atmosphere. Also X-rays are under study within this thesis. The most energetic electromagnetic radiation is called gamma rays, which interact rather weakly with matter. These photons are generated at the very extremest of conditions in the Universe.

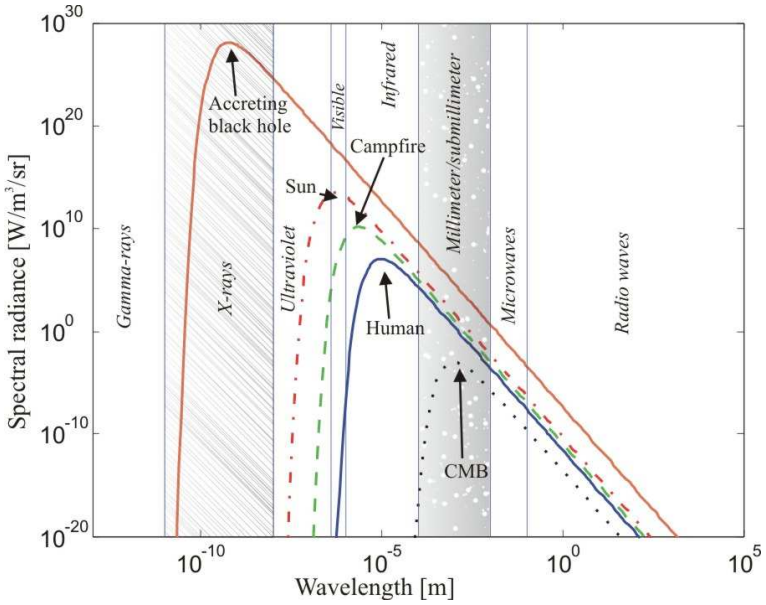

Figure 1: The electromagnetic spectrum. The curves correspond to the blackbody spectra of the cosmic microwave background (T = 3 K), a human (T = 310 K), a campfire (T = 1200 K), the Sun (T = 6000 K), and an accreting black hole (T=5 million K). The shaded regions are of relevance to the work presented here.

1.2 Detection methods

The detection of radiation relies on the interaction of electromagnetic radiation with matter. The detection methods are commonly divided to two main categories: Coherent detection and incoherent (or direct) detection. In the former case, both the amplitude and the phase information of the incoming radiation is detected, while in the latter only the other quantity, usually the amplitude, is measured.

Most common type of incoherent detectors are photon detectors, which respond directly to absorbed photons. An absorbed photon generates bound charge carriers through the photoelectric effect, and the resulting signal is either a chemical change, modulation of the electrical current through the device, or the primary charge collected directly with a charge sensitive amplifier. Photon detectors yield information on the energy and the absorption rate of the incident photons. These devices are used throughout the gamma, X-ray, ultraviolet, visible, and infrared regions. A long wavelength cut-off in the far-infrared is imposed on photodetectors by the energy required to create primary excitations.

Another class of incoherent detectors are thermal detectors. In thermal detectors, the operation is based on the absorption and thermalization of photons. Usually the resulting temperature change modulates an electrical property of the device, such as resistance. An attractive feature of thermal detectors is that they are extremely broad band devices, as the energy of the primary excitation, the phonon, is very small. Thermal detectors are thus used all the way from gamma rays to microwaves, and are the focus of this work.

In coherent detectors, the detection is based on the accelerating effect of the electric field of the incident radiation to the electrons in the detector. At frequencies where low noise amplifiers exist ($\lesssim 200$ GHz), the signal is amplified prior to detection. At higher frequencies a method called heterodyning is used where the incoming electromagnetic field is mixed with a coherent local oscillator signal, and the resulting beat frequency, often called the intermediate frequency (IF), is amplified while phase information of the photons is preserved. This type of detectors are used primarily from the submillimeter to radio wavelengths, but also in the infrared. Notably, a coherent detection system can incorporate incoherent detectors as mixing elements.

Comparison of the different detection techniques is difficult as it is impossible to establish a single performance marker for the various methods. The application determines the best option: for instance, if high resolution spectroscopy in the millimeter wave region is the application, incoherent detectors are typically not a good choice. Likewise, if one desires to do broad

band radiometry, incoherent detectors outperform coherent detectors. Simultaneously, one has to bear in mind technological constraints: while cooling to 100 mK is considered acceptable for high resolution X-ray astrophysics, a portable X-ray fluorescence analyzer is unlikely going to house an adiabatic demagnetization refrigerator. A brief summary of various detection methods from visible to infrared is collected to table 1. Only one parameter is quoted as a figure of merit, which is the noise equivalent power (NEP), discussed in more detail in Section 2. This parameter is relevant for radiometric applications when detecting changes in the incident flux of photons.

1.3 Figures of merit

A perfect radiation detector would preserve all the information contained in the incoming flux of photons. The important figures of merit are

i) *Noise* of the detector. In the ideal case, the internal noise of the detector should not hinder the accuracy of the measurement. The limiting accuracy in the ideal detector is due to statistical fluctuations in the photon flux itself.

ii) *Linearity.* A linear detector produces an output signal which is proportional to the input power or energy.

iii) *Quantum efficiency.* This is given by the ratio of the number of absorbed photons to those of the incident photons, $\eta = N_{\mathrm{abs}}/N_{\mathrm{i}}$. Ideally, all the photons are absorbed, and quantum efficiency is unity. The quantum efficiency depends on the energy of the photons, and should remain relatively unchanged over the range of energies to be detected.

iv) *Dynamic range.* A large dynamic range is required especially when detecting small variations in signal on top of a large (constant) background signal.

v) *Speed.* A fast detector is needed if rapid changes in the incident power are to be detected.

vi) *Scalability* to large arrays. Imaging detectors usually use a large number of pixels to form an image.

vii) *Dissipation.* Especially in cryogenic detectors the power consumption is critical, as the available cooling power is limited at low temperatures.

The sensitivity of detectors in the visible and infrared spectral regions is often expressed in terms of *Noise Equivalent Power*, or NEP, from the expression for signal-to-noise ratio

$$\frac{S}{N} = \frac{\eta P_{\rm opt}}{\rm NEP}\sqrt{\tau_{\rm int}}, \tag{1}$$

where $\tau_{\rm int}$ is the post detection integration time and $P_{\rm opt}$ is the signal power. Another useful figure of merit for infrared detectors is the *Noise Equivalent Temperature Difference*, or NETD, which expresses the minimum detectable change in the target blackbody temperature. A general form is given by

$$\text{NETD} = \frac{\text{NEP}}{\eta \partial P_{\rm opt}/\partial T \sqrt{\tau_{\rm int}}}, \tag{2}$$

where $P_{\rm opt}$ is the blackbody power incident on the detector given by

$$P_{\rm opt} = \int_{\lambda_1}^{\lambda_2} LA\Omega \; d\lambda = \int_{\lambda_1}^{\lambda_2} \frac{2hc}{\lambda^5 (e^{hc/\lambda k_{\rm B} T} - 1)} \lambda^2 \; d\lambda, \tag{3}$$

and diffraction limited throughput $A\Omega = \lambda^2$ of a single mode is assumed. In the Rayleigh-Jeans limit when $hc/\lambda \ll k_{\rm B}T$, Eq. (3) simplifies to

$$P_{\rm RJ} = 2k_{\rm B}T\Delta\nu, \tag{4}$$

where $\Delta\nu = c(\lambda_2 - \lambda_1)/(\lambda_1\lambda_2)$. Thus, the expression for NETD becomes

$$\text{NETD}_{\rm RJ} = \frac{\text{NEP}}{2\eta k_{\rm B}\Delta\nu\sqrt{\tau_{\rm int}}}. \tag{5}$$

In many situations, including comparisons with coherent detectors, NETD is a rather convenient method to compare detector sensitivity.

In coherent detection methods, such as heterodyne receivers or HEMT tuned RF receivers, the sensitivity is often expressed in terms of receiver noise temperature $T_{\rm N}$. The relation between $T_{\rm N}$ and NEP is

$$\text{NEP} = k_{\rm B}T_{\rm N}\sqrt{\Delta\nu}, \tag{6}$$

where $\Delta\nu = 2\Delta f_{\rm IF}$ for double sideband receiver and $\Delta\nu = \Delta f_{\rm IF}$ for single sideband receivers where $\Delta f_{\rm IF}$ is the bandwidth of the intermediate frequency amplifier. The noise temperature of a receiver can be either limited by the noise of the amplifier, the noise of the mixer, noise in the input power, or, ultimately, by the so called quantum noise. Quantum noise arises from the Heisenberg's uncertainty relation according to which the accuracy with which

one can measure the energy and the arrival time of the incoming photon is limited to

$$\Delta E \Delta t \gtrsim \hbar. \tag{7}$$

For the measurement of power, the uncertainty becomes $\Delta P = h\nu/\Delta t$, which corresponds to a noise temperature $T_{\mathrm{N,QL}} = h\nu/k_{\mathrm{B}}$.

This limit is not imposed on incoherent detectors which do not detect the phase of the incoming radiation. One way to compare the performance of coherent and incoherent detectors is to study the background limited noise level (often called as BLIP, from Background Limited Performance) as a function of the ratio $h\nu/k_{\mathrm{B}}T$. The limiting NEP for a incoherent detector observing a single mode is given by

$$\mathrm{NEP}_{\mathrm{BLIP,d}} = h\nu\sqrt{\Delta\nu}\sqrt{\frac{n_0(1+\eta_{\mathrm{d}}n_0)}{\eta_{\mathrm{d}}}}, \tag{8}$$

where $n_0 = (e^{h\nu/k_{\mathrm{B}}T} - 1)^{-1}$ is the background occupancy number and η_{d} is the total quantum efficiency of the detector. For a coherent detector, the background limited performance is given by

$$\mathrm{NEP}_{\mathrm{BLIP,c}} = h\nu\sqrt{\Delta\nu}\frac{(1+m\eta_{\mathrm{c}}n_0)}{\eta_{\mathrm{c}}}, \tag{9}$$

where η_{c} is the quantum efficiency of the coherent detector. The constant $m = 1$ for single sideband mixer or an amplifier, and for double sideband mixer $m = 2$ [1]. A comparison is shown in Fig. 2.

This thesis focuses on the development and optimization of thermal detectors for two wavelength ranges: for the X-ray region and for the submillimeter to millimeter wavelength range, which are of particular interest for several reasons. X-ray astronomy is a blooming field of astrophysics and several ambitious space borne observatories, such as NASA's *Constellation X* [2], and European Space Agency's *XEUS* missions [3] which will study energetic phenomena at the far reaches of our Universe with an unprecedented sensitivity. Ground-based applications of high resolution X-ray spectroscopy are in semiconductor industry where the detector technology benefits process control, and also in materials analysis where the high resolution enables the detection of chemical shifts in the fluorescence spectra of elements.

The submillimetre wave range is interesting as it contains a huge number of vibrational and rotational spectra of molecules, implying a variety of spectroscopy applications. Long range terrestrial applications are limited by the strong attenuation of submillimetre waves in the lower atmosphere, a reason why ground based submillimetre astronomy is carried out at mountain tops

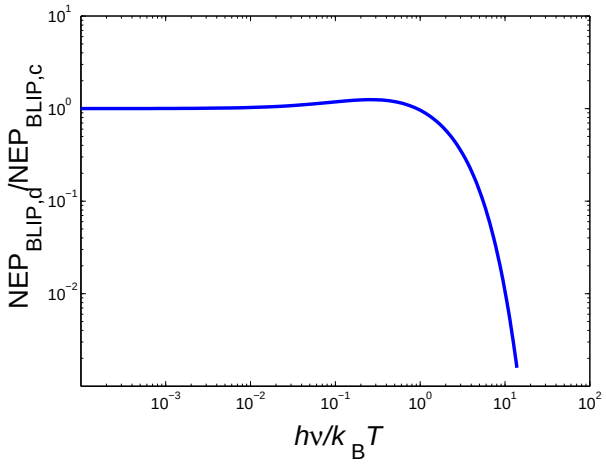

Figure 2: A comparison of the background limited performance of a incoherent detector and a coherent detector. Incoherent detectors outperform coherent detectors when $h\nu/k_{\mathrm{B}}T \gtrsim 1$, which corresponds to $\nu \approx 2$ THz for a 300 K blackbody and $\nu \approx 60$ GHz for a 3 K blackbody. The calculation assumes $\eta_{\mathrm{d}} = 0.1$ and $\eta_{\mathrm{c}} = 0.5$. Also an identical bandwidth $\Delta\nu$ is assumed.

and from balloons. Cosmologists observe the echoes of the Big Band in the submillimetre waves, as its radiance peaks at submillimetre waves and the clutter from foreground objects, such as planetary and galactic dust, is low. An unprecedented view to the infant Universe will open within a few years with the commissioning of the *Herschel-Planck* mission [4].

Beyond *Herschel-Planck*, future science objectives require the development of much larger image forming incoherent detector arrays than are in use today. The large array size, combined with stringent sensitivity requirements pose a significant challenge for the experimentalist. Closer to earth, a number of applications are envisioned, one of which is the passive imaging of concealed weapons, explosives, or other contraband, under clothing. The ability of passing relatively unobscured through dielectric objects combined with the short wavelength allows the construction of cameras with a reasonable aperture size.

INCOHERENT						Ref.
Detector type	operating temperature	λ range	NEP [W/Hz$^{1/2}$]	Array size	Power /pixel	
Photovoltaic	$\sim$ 100 K	1 μm $\sim$ 2.5 μm	10^{-17}	$> 10^6$	$\sim$ 1 nW	[5]
	$\sim$ 2 K	110 μm	10^{-17}	10^0		[6]
Thermal	$\sim$ 300 K	8 μm - 12 μm	10^{-13}	10^5	$\sim$ 100 nW	[7]
	$\sim$ 300 K	2 mm	10^{-11}	10^1	$\sim$ 400 μW	This work[1]
	4.2 K	2 μm $\sim$ 5 mm	10^{-13}	10^1		[8]
	4.2 K	150 μm-660 μm	10^{-14}	10^0	20 nW	This work[1]
	$\sim$ 370 mK	100 μm 5 mm	10^{-17}	10^1	10 pW	[9]

COHERENT						
HEMT TRF	$\sim$300 K	> 1.5 mm	10^{-14}	10^3	$\sim$1 W	[10]
	20 K		10^{-16}	10^1	10 mW	[11]
Schottky	$\sim$300 K	~ 600 μm	10^{-15}	10^1	1 mW	[12]
Schottky	$\sim$300 K	~ 120 μm	10^{-14}	10^1	1 mW	[12]
SIS	4.2 K	> 220 μm	10^{-16}	10^1	$\sim$1 μW	[12]
HEB	4 K - 20 K	> 120 μm	10^{-15}	10^0	$\sim$100 nW	[13, 14]

Table 1: A comparison of detection methods from the infrared to millimetre-wave spectral ranges. [1]Electrical measurements.

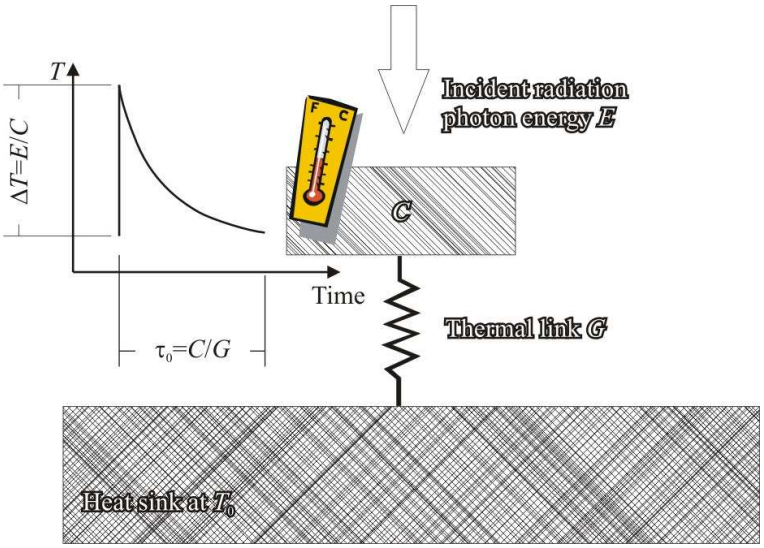

Figure 3: A simplified diagram of the operating principle of a thermal detector. An incident photon causes a temperature rise in a thermally isolated heat capacity (denoted by C). The heat escapes via a thermal link G to the heat sink in a time scale determined by the thermal time constant $\tau_0 = C/G$.

2 Thermal detectors

2.1 Operating principle

Thermal detectors measure energy. The absorbed energy results in a temperature rise, given by $\Delta T = E/C$, where E is the input energy, and C is the total heat capacity of the absorbing system. In a detector, the temperature rise ΔT is typically transformed to a suitable measurable electrical parameter, such as the dielectric constant, electrical resistivity, or inductance. When used to measure the energy of individual incident photons, thermal detectors are called calorimeters (from latin *calor*=heat), and if changes in the incident flux of photons (power) is measured, the devices are called bolometers (from greek *bolē*=ray). At submillimeter wavelengths the rate of photons is very large compared to the typical time constant of a detector, and thus devices are called bolometers, whereas in the X-rays, it is possible to use calorimetric mode as the rate of photons is small.

Thermal detectors are divided to several subgroups depending on the way the signal (heat) is transformed to a measurable signal. The most common types are pyroelectric and resistive thermal detectors. In the former, the signal is produced by the polarization of the detector material due to the

temperature change. In the latter, the electrical resistivity of the material is modified due to a change in the temperature. The pulse response of a thermal detector to a photon is shown in Fig. 3. The absorbed photon causes a sharp rise in temperature with the rise time limited by the time it takes for the photon energy to thermalize through the heat capacity C. The pulse is followed by an exponential fall time to the steady state condition.

The behaviour of a calorimeter can be obtained from

$$C(T)\frac{dT}{dt} + P_{\text{out}} = P_{\text{in}} \tag{10}$$

where the first term on the left describes the time rate of change of heat stored to the heat capacity of the sensor, and the second term is the power flowing out of the detector, while the term on the right side is the input power, which consists of contributions from the bias power, optical power and the noise power. The power flowing out of the detector is given by [15]

$$P_{\text{out}} = \frac{\int_{T_0}^{T_{\text{d}}} \kappa(T)dT}{\int_0^{x_d}[A(x)]^{-1}dx}, \tag{11}$$

where A is the cross section of the link, T_{d} is the temperature of the detector (at $x = x_{\text{d}}$), T_0 is the temperature of the heat sink (at $x = 0$) and the thermal conductivity $\kappa(T)$ depends on the characteristics of the link. In a metallic (normal state) link at low temperatures ($T \ll \Theta_{\text{D}}$) the heat transport is mainly by the electron gas in the metal, and thus the thermal conductivity is given by Wiedemann-Franz law, $\kappa(T) = LT/\rho_{\text{n}}$ where $L = 2.45 \cdot 10^{-8}$ V^2/K^2 is the Lorentz number and ρ_{n} is the resistivity of the metal. In the case of a crystalline dielectric link the heat is transported by phonons in the lattice. The crystalline structure of the material has a strong influence on the thermal conductivity, but typically $\kappa(T) = aT^b$ with a a constant and $b \sim 2$. In superconductors, the charge carriers, known as Cooper pairs, all sit in a low energy state of zero entropy, which is separated by an energy gap $\Delta E = 1.76 k_{\text{B}} T_{\text{c}}$ from the states of the single, unpaired electrons. Only broken pairs (single electrons) can carry entropy (and thus heat), and their density has an exponential dependence on temperature. The thermal conductivity of a superconducting link coincides with the thermal conductivity of a metallic link when $T \to T_{\text{c}}$, the critical temperature of the superconductor. Slightly below T_{c}, the electronic contribution $\kappa(T) = \kappa_0 e^{-\Lambda T_{\text{c}}/T}$ with $\kappa_0 = LTe^{\Lambda}/\rho_{\text{n}}$, and $\Lambda \approx 1.76$. In disordered superconductors (and at intermediate temperatures of a few K), also the lattice conductivity has a significant effect on the thermal transport. In this case the temperature dependence is rather difficult to estimate.

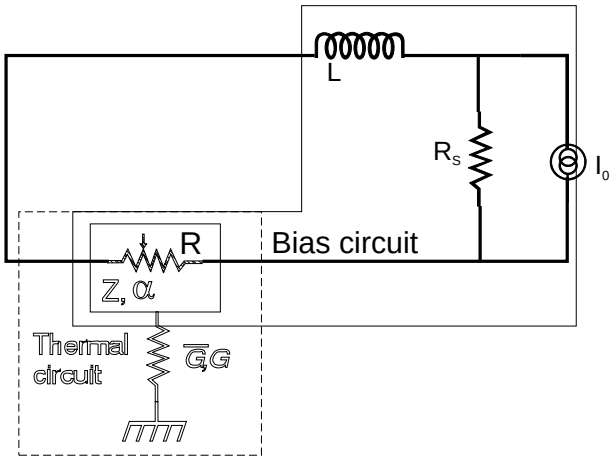

Figure 4: The electro-thermal circuit of a bolometer. The circuit is divided to two major subparts: the electrical circuit (solid lines) and the thermal circuit (open lines). The interplay between the electrical and thermal circuits takes place in the bolometer.

A typical bias circuit of a bolometer is shown in Fig. 4. It can be divided to the thermal circuit, described by heat capacity C and thermal conductances G and $\overline{G}$, defined below, and an electrical circuit consisting of a bias supply V with a source impedance $Z_{\rm S}(\omega) = R_{\rm S} + i\omega L$.

Considering a general case, where the power flow to the heat sink is given by

$$P_{\rm out} = K(T^n - T_0^n), \tag{12}$$

where K is a constant which depends on materials parameters and the geometry of the link, the equation for a bolometer with a bias point resistance of $R = V/I$ absorbing a time-varying optical signal $P_{\rm opt} = P_{\rm o}e^{i\omega t}$ becomes

$$C\frac{d(\delta T e^{i\omega t})}{dt} + K(T^n - T_0^n) + G\delta T = P_{\rm bias} + P_{\rm o}e^{i\omega t} + \frac{dP_{\rm bias}}{dT}\delta T, \tag{13}$$

where δT is used to denote the temperature change due to the signal power. Equating the steady state components of the equation yields

$$P_{\rm bias} = K(T^n - T_0^n), \tag{14}$$

from which one can obtain the result for the average operating temperature of the bolometer, given by

$$T = \frac{P_{\rm bias}}{\overline{G}} + T_0 \tag{15}$$

where an average thermal conductance $\overline{G}$ is defined by

$$\overline{G} = \frac{K(T^n - T_0^n)}{T - T_0} = \frac{P_{\mathrm{bias}}}{\left(\frac{P_{\mathrm{bias}}}{K} + T_0^n\right)^{1/n} - T_0}. \tag{16}$$

The change in input signal power modifies the bias dissipation, an effect described by the last term in Eq. (13). This effect is commonly known as *electrothermal feedback* (ETF). Taking a closer look at the temperature change we obtain

$$\delta T = \frac{P_o}{G + i\omega C - dP_{\mathrm{bias}}/dT} \tag{17}$$

where $G = dP/dT \approx nKT^{n-1}$ is the dynamic thermal conductance. Now, considering the electrothermal term

$$\frac{dP_{\mathrm{bias}}}{dT} = \frac{dP_{\mathrm{bias}}}{dR}\frac{dR}{dT} = -I^2\left[\frac{R - Z_{\mathrm{S}}(\omega)}{R + Z_{\mathrm{S}}(\omega)}\right]\frac{\alpha R}{T} = -\frac{P_{\mathrm{bias}}\alpha}{T}\beta(\omega), \tag{18}$$

where we have used $\alpha \equiv d\log R/d\log T$ the dimensionless temperature coefficient of resistance for the thermometer, and $\beta(\omega) \equiv [R - Z_{\mathrm{S}}(\omega)]/[R + Z_{\mathrm{S}}(\omega)]$ the effect of the bias circuit on the ETF. Taking into account the thermal cut-off of the bolometer, the frequency-dependent loop gain is defined as

$$\mathcal{L}(\omega) \equiv \frac{P_{\mathrm{bias}}\alpha}{GT}\frac{\beta(\omega)}{\sqrt{1 + \omega^2\tau_0^2}} = \mathcal{L}_0\frac{\beta(\omega)}{\sqrt{1 + \omega^2\tau_0^2}}, \tag{19}$$

where $\tau_0 = C/G$ is the intrinsic thermal time constant of the bolometer. The electro-thermal loop gain describes the effect of changing input power to the bias power of the detector. For positive bolometers with $\alpha > 0$ the loop gain is positive for current bias (since $\mathrm{Re}[\beta(\omega)] > 0$) and negative for voltage bias (as $\mathrm{Re}[\beta(\omega) < 0]$). Negative bolometers will not be discussed within the scope of this thesis. For metallic bolometers operated at room temperature $\alpha \sim 1$ and the loop gain is typically small ($\mathcal{L}_0 \lesssim 1$) so that the role of ETF is negligible. On the contrary, superconducting detectors with $\alpha \sim 100$ and G some three orders of magnitude smaller than for room temperature devices can have large loop gain ($\mathcal{L}_0 \sim 50$), so that ETF plays a significant role in the detector characteristics.

For measurement purposes, it is worthwhile to notice that $\mathcal{L}$ can also be expressed as

$$\mathcal{L}(\omega) = \frac{dR/R}{dP/P} = \frac{P}{R}\frac{d(V/I)}{d(VI)} = \frac{Z(\omega) - R}{Z(\omega) + R}\beta(\omega), \tag{20}$$

where $Z(\omega) = dV/dI$ is the dynamic (electrical) impedance of the bolometer and as $\omega \to \infty$, $Z = R$ since signals faster than the time constant do not affect the operating point of the bolometer [16].

A major impact of the ETF is that the bolometer time constant is reduced from τ_0 to $\tau_{\rm eff} = \tau_0/[1 + \beta(0)\mathcal{L}_0]$.

A common way of biasing bolometers is to drive a constant current I_0 through a parallel combination of the bolometer and the load resistor $R_{\rm S}$. As long as $R_{\rm S} \ll R$, the bolometer is effectively voltage biased. The responsivity of a voltage biased bolometer can be derived as follows: The current responsivity is defined as $S_{\rm I} \equiv dI/dP_{\rm o} = (dI/dR)(dR/dT)(dT/dP_{\rm o})$. Now, using Eqs. (17), (18) and (20) we can write

$$\left|\frac{dT}{dP_{\rm o}}\right| = \frac{1}{G}\left|\frac{1}{1 + i\omega\tau_0 + \mathcal{L}_0\beta}\right| = \frac{1}{G}\frac{1}{1+\beta\mathcal{L}_0}\frac{1}{\sqrt{1+\omega^2\tau_{\rm eff}^2}}. \tag{21}$$

Next, we note that $(dR/dT) = \alpha R/T$. To calculate the total derivative dI/dR we need to take into account the effect of the bias circuit on dI. At zero frequency, the voltage across the bolometer is $V = I_0 R_{\rm S} R/(R_{\rm S} + R)$, while the current is $I = I_0 R_{\rm S}/(R_{\rm S} + R)$. Thus, $dI/dR = -I_0 R_{\rm S}/(R_{\rm S} + R)^2 = -I(\beta + 1)/(2R)$. Using these results, the current responsivity becomes

$$\begin{aligned} S_{\rm I}(\omega) &= \frac{I\alpha R}{GT}\frac{1+\beta}{2}\frac{1}{1+\beta\mathcal{L}_0}\frac{1}{\sqrt{1+\omega^2\tau_{\rm eff}^2}} \\ &= -\frac{1}{V}\frac{(1+\beta)\mathcal{L}_0}{2(1+\beta\mathcal{L}_0)}\frac{1}{\sqrt{1+\omega^2\tau_{\rm eff}^2}}. \end{aligned} \tag{22}$$

In the limiting case at $\omega = 0$ with $\beta = 1$ (perfect voltage bias) and $\mathcal{L}_0 \gg 1$,

$$S_{\rm I}(0) = -\frac{1}{V}. \tag{23}$$

A similar treatment can be carried out for a current biased bolometer, when $R_{\rm S}$ is in series with the bolometer. This derivation yields

$$S_{\rm V}(\omega) = \frac{1}{I}\frac{(1-\beta)\mathcal{L}_0}{2(1+\beta\mathcal{L}_0)}\frac{1}{\sqrt{1+\omega^2\tau_{\rm eff}^2}}, \tag{24}$$

which yields in the limit $\omega = 0$, $\beta = -1$ and $\mathcal{L}_0 \gg 1$

$$S_{\rm V}(0) = -\frac{1}{I}. \tag{25}$$

Next, we shall summarize the various sources of noise in thermal detectors. The limiting noise source in a thermal detector arises from the

spontaneous exchange of energy between the heat sink and the detector heat capacity C across the thermal link G. It can be shown, that this energy exchange leads to a current noise at the output of the voltage biased detector given by the so-called thermal fluctuation noise (TFN), also known as phonon noise [15]

$$\delta I_{\mathrm{TFN}} = \frac{\sqrt{4\gamma k_{\mathrm{B}} T^2 G}}{2V} \frac{(1+\beta)\mathcal{L}_0}{(1+\beta\mathcal{L}_0)} \frac{1}{\sqrt{1+\omega^2\tau_{\mathrm{eff}}^2}} \tag{26}$$

where γ describes the effect of the temperature gradient across the thermal link with $\kappa \propto T^b$ between the sensor and the heat sink [15] in the diffusive limit

$$\gamma = \frac{(b+1)\left({T_{\mathrm{c}}}^{b+3} - {T_{\mathrm{c}}}^{-b}{T_0}^{3+2\,b}\right)}{(3+2\,b)\,{T_{\mathrm{c}}}^2\left({T_{\mathrm{c}}}^{b+1} - {T_0}^{b+1}\right)} \approx \frac{b+1}{2b+3}, \tag{27}$$

where the approximation is valid when $T_{\mathrm{c}} \gg T_0$.

Another noise contribution is due to the Johnson noise, given by

$$\delta I_{\mathrm{JN}} = \frac{\sqrt{4k_{\mathrm{b}}TR^{-1}}}{2} \frac{1+\beta(\omega)}{1+\beta(\omega)\mathcal{L}_0} \frac{\sqrt{1+\omega^2\tau_0^2}}{\sqrt{1+\omega^2\tau_{\mathrm{eff}}^2}}. \tag{28}$$

It is often stated that the Johnson noise is *suppressed* by the ETF, while more appropriate would be to say that the Johnson noise is *not amplified* by the electro-thermal gain of the sensor. Thus, in the output of the sensor, the relative contribution of Johnson noise compared to TFN is smaller at frequencies below τ_0^{-1}.

Additionally, there are contributions from the noise of the amplifier, as well as from internal thermal fluctuations which arise from the distributed internal thermal resistance of the detector [17, 18], and finally, as will be shown in Section 5, excess noise due to fluctuation superconductivity above T_{c}.

3 Antenna-coupled microbolometers

3.1 Room temperature antenna-coupled microbolometers

Antenna-coupled microbolometers can extend the wavelength limits of bolometers from infrared to the millimetre-wave range [19, 20, 21, 22]. This Section briefly summarizes the results obtained with titanium air-bridge microbolometers, coupled to a full-wave dipole antenna.

The main benefit of antenna coupling is the fact that the thermally active element can be made much smaller than the wavelength of the incoming radiation. This is of especial importance when millimetre-waves are detected, as the required size of the bolometer becomes prohibitingly large, as the area of the absorbing element scales as λ^2. Increased area results to a large heat capacity, and thus slow time constant, as the thermal conductance G is set by the sensitivity requirement. Since the thermal time constant of the antenna-coupled microbolometers is very short (of the order 1 μs), there is much room to improve the thermal isolation. All of the power received by the antenna is dissipated to the bolometer bridge, given that the antenna and the bolometer impedances are matched.

Our approach to improve the thermal isolation is the removal of the heat conductance to the substrate by fabricating the bolometer to a free standing bridge structure, and coupling the bolometer to an antenna with relatively high input impedance Z_{ant} since $G \propto 1/Z_{\mathrm{ant}}$.

After a survey of lithographic antenna literature, we selected a full-wave dipole although dipoles on dielectric substrates do suffer from losses to back lobes. The most attractive property was the possibility of obtaining feeding point impedances Z_{ant} in excess of 200 Ω [23]. A more thorough study beyond the scope of this work could utilize other antennae with better beam characteristics, combined with planar impedance transformers that could increase the input impedance even further. The operating frequency was chosen to be 160 GHz which is a trade-off between atmospheric transmission and 300 K blackbody radiance, with the former decreasing with frequency while the radiance increases.

One important consideration in resistive bolometers is the $1/f$ noise. Although this noise source can be avoided by modulating the optical signal at a frequency above the knee frequency where $1/f$ noise equals the Johnson noise, the knee frequency might be too high for practical modulation methods. The $1/f$ noise in a resistor is given by

$$V_{1/f}^2(f) = V^2 z f^r = V^2 \alpha_H n_{\mathrm{e}} \Omega f^r, \tag{29}$$

where $r \simeq -1$, V is the voltage across the detector, the $1/f$ noise parameter is $z = \alpha_{\mathrm{H}}/(n_{\mathrm{e}}\Omega)$, with α_H the Hooge parameter [24], n_{e} the mobile charge carrier density, and Ω the volume of the bolometer. It is crucial for a resistive antenna-coupled microbolometer to have a low $1/f$ noise since their volume is much smaller than in typical surface-absorbing infrared microbolometers. We studied the $1/f$ spectra from three materials: platinum, niobium, and titanium. Another important factor is the temperature coeffcient of resistance which should be as large as possible. The results from the materials characterisation are collected in Table 2. Based on these findings we chose Ti as the bolometer material.

Material	TCR (α/T) [%/K]	r	z [Hz$^{-(r+1)}$]
Ti	0.31	-1.22	$7{\cdot}10^{-13}$
Nb	0.045	-1.13	$13{\cdot}10^{-13}$
Pt	0.19	-0.9	$24{\cdot}10^{-13}$

Table 2: Results for the temperature coefficient of resistance (TCR) and the $1/f$ noise for Ti, Nb and Pt.

The bolometers were fabricated on a 525 μm thick nitridized high resistivity (10 kΩcm) silicon wafer. The fabrication details are very similar to those used in the study of the superconducting Nb bolometers, described in paper V. The main difference was the incorporation of a separate metallization layer for the full-wave dipole antenna. The antenna layer was patterned using electron beam lithography and a double layer electron resist. The Au was grown using ultra-high vacuum (UHV) electron gun evaporation to a thickness of 200 nm, and a lift-off in acetone followed. A second double-layer electron resist was spun on the wafer, and the bolometer bridge was patterned. After development, we used a short O_2 plasma etch to remove resist residuals from the antenna-bolometer contact region prior to the deposition of the Ti bolometer film. The Ti was evaporated to a thickness between 180

CF_4 flow	7.35 sccm
O_2 flow	2.0 sccm
RF power	245 mW/cm^2
Pressure	35 mTorr - 70 mTorr
Time	$\sim$ 2 min

Table 3: Bridge release RIE parameters.

nm and 200 nm, followed by a lift-off. The release of the bridge was carried out as with in the superconducting Nb bolometers using reactive ion etching (RIE) with oxygen and carbon tetrafluoride (CF_4) at a relatively high pressure between 35 mTorr and 70 mTorr. The etch started at the lower pressure in order to break the surface. After $\sim$ 1 minute the pressure was raised to 75 mTorr which results to an isotropic etch which removes the SiN underneath the bridge. The etch parameters are tabulated in Table 3. The resulting bolometer structure is shown in Fig. 5.

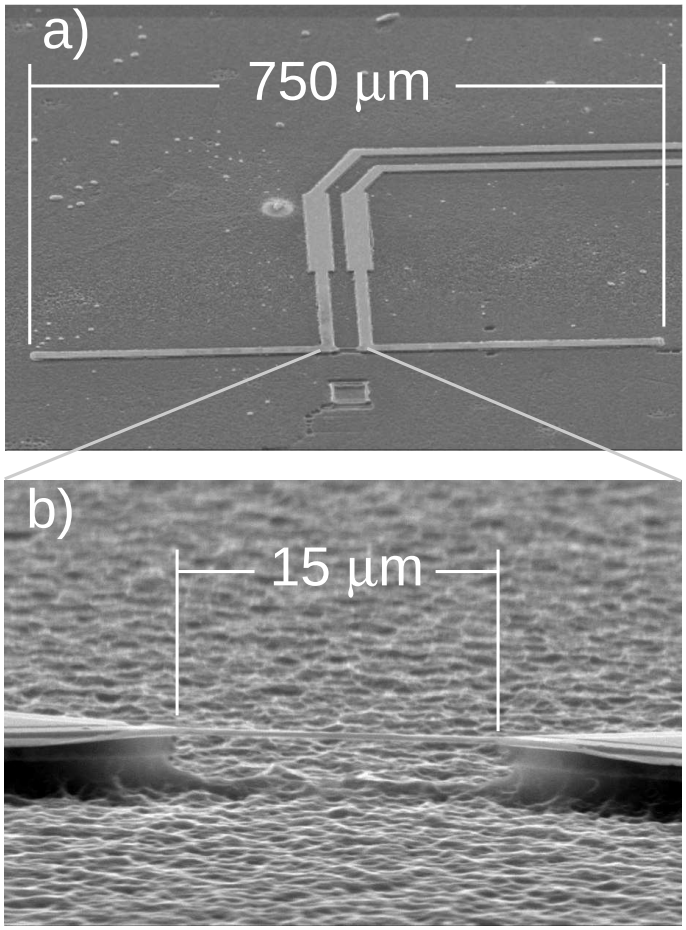

Figure 5: A SEM image of the 15 μm $\times$ 1 μm $\times$ 180 nm Ti bridge bolometer, with a) an overview of the bolometer and the antenna. The widenings in the low frequency measurement lines serve as $\lambda/4$ low-pass filters to prevent RF loss to the lines. b) A closeup of the antenna feed, showing the suspended bridge.

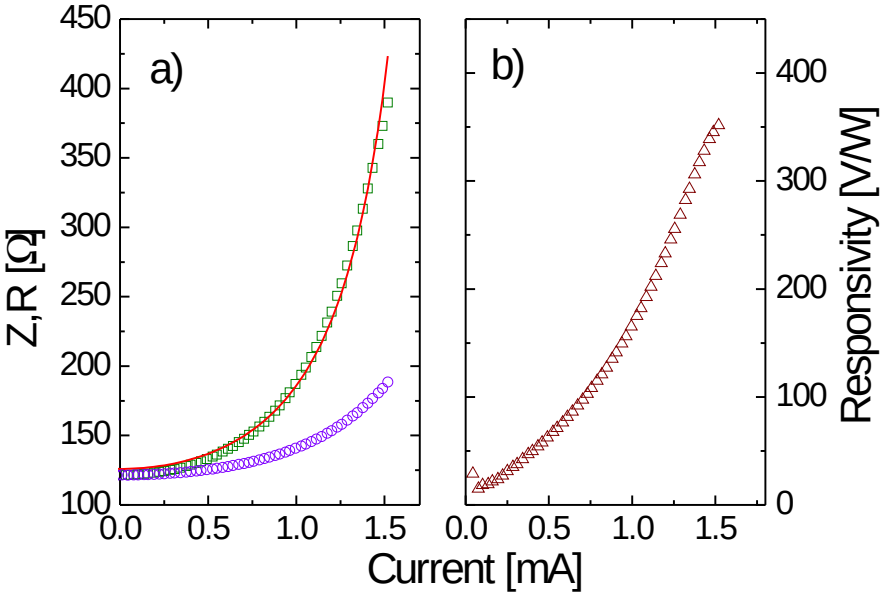

Figure 6: a) The resistance R (circles) and differential resistance Z (squares) of the Ti bridge as a function of the bias current. A fit (line) to the $Z(I)$ curve yields a value $G = 3$ μW/K for the thermal conductivity according to Eq. (30). b) The measured electrical responsivity of the bolometer.

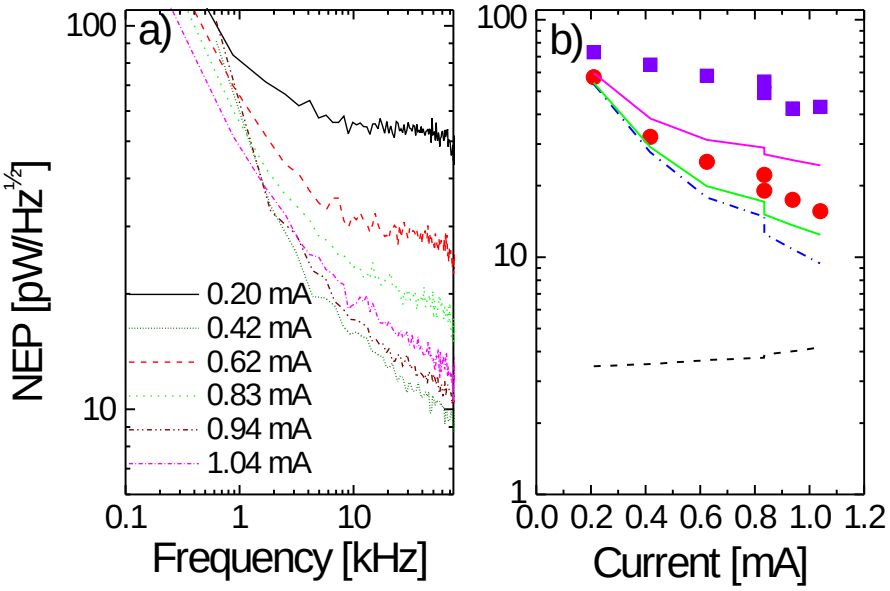

Figure 7: a) The spectrum of NEP at various bias currents, indicated in the legend of the figure. b) The NEP at 1 kHz (squares) and at 10 kHz (circles). The two solid lines represent the expected NEP with contributions from thermal fluctuation noise, Johnson noise and $1/f$ noise with $z = 7 \cdot 10^{-13}$. The dashed line represents the thermal fluctuation noise limit, and the dash-dotted line is the contribution of the Johnson noise.

The electrical performance of the current biased bolometer was characterized by measuring its $I(V)$ and differential resistance $Z = dV/dI$ *in vacuo*. The differential resistance measurement was carried out using the lock-in technique. The results are shown in Fig. 6. The voltage responsivity of the bolometer was determined using Eqs. (20) and (24). The $Z(I)$ curve can be used to fit the thermal conductivity G using

$$Z(I) = R_0 \left[\frac{G^2 - GI^2\alpha T^{-1} R_0 + 2I^4\alpha^2 T^{-2} R_0^2}{(2I^2\alpha T^{-1} R_0 - G)^2} \right], \tag{30}$$

which is obtained from $V(I) = R(I)I = IR_0G/(G - \alpha T^{-1} I^2 R_0)$ with where R_0 stands for the zero-bias resistance.

The noise of the bolometer was determined by measuring the noise voltage across the bolometer using a pair of low noise preamplifiers with a gain of

1000 connected to the inputs of a correlation FFT spectrum analyzer. When used in the correlation mode, the noise contributions from the preamplifiers are eliminated, and the noise of the bolometer can be determined accurately. Combined with the results from the responsivity measurements, the electrical NEP of the bolometer is obtained. The results are shown in Fig. 7. The $1/f$ noise is higher than expected, which might be due to the RIE process which can increase the density of impurities in the Ti. At 10 kHz, the device is almost limited by the Johnson noise with a NEP=15 pW/$\sqrt{\text{Hz}}$. However, at the more practical chopping frequency of 1 kHz the NEP is at best 42 pW/$\sqrt{\text{Hz}}$.

In the final stage of characterization we measured the optical response of the bolometer to a millimetre-wave signal. As a source, a Gunn oscillator with a frequency doubler was used. The source could be tuned from ∼150 GHz up to about 180 GHz. The output of the source was connected to a pyramidal horn antenna. A rotating chopper was placed in front of the horn to modulate the incident power on the bolometer at a chopping frequency of $\sim$ 700 Hz. The bolometer was attached to the backside of a 10 mm diameter hemispherical silicon lens , and centred by visual inspection to an accuracy of ∼50 μm. The bolometer/lens combination was placed 28.5 cm from the horn. The bolometer was again current biased, and the voltage across the bolometer was connected to a low noise laboratory preamplifier with a voltage gain of 10 000. Bandwidth of the preamplifier was limited from 30 Hz to 1000 Hz, and the output was connected to the signal input of a lock-in amplifier. The reference signal was the 0-5 V TTL from the chopper, which was connected to the reference input of the lock-in amplifier.

A frequency response measurement was performed in order to verify that the device indeed responds at the design frequency of 160 GHz. This measurement was carried out by placing the bolometer facing the horn antenna, and adjusting the oscillator to different frequency settings. The output power from the waveguide was measured using a calibrated total power meter[1]. The results calibrated against the Dorado DPM-2 are shown in Fig. 8 (a). Clearly, there is a strong response at 160 GHz, as expected. More points below 150 GHz would be needed to get an accurate figure for the bandwidth of the device. If using a typical value for lithographic dipoles of about 30 % bandwidth (3 dB) around the centre frequency, the response indicates a centre frequency of ∼144 GHz. This shift in the centre frequency can be caused by impedance mismatch between the antenna and the bolometer. As the final optical measurement we measured the response of the bolometer to the millimetre-wave signal as a function of the bias current. The source

[1]Dorado DPM-2 Total Power Meter

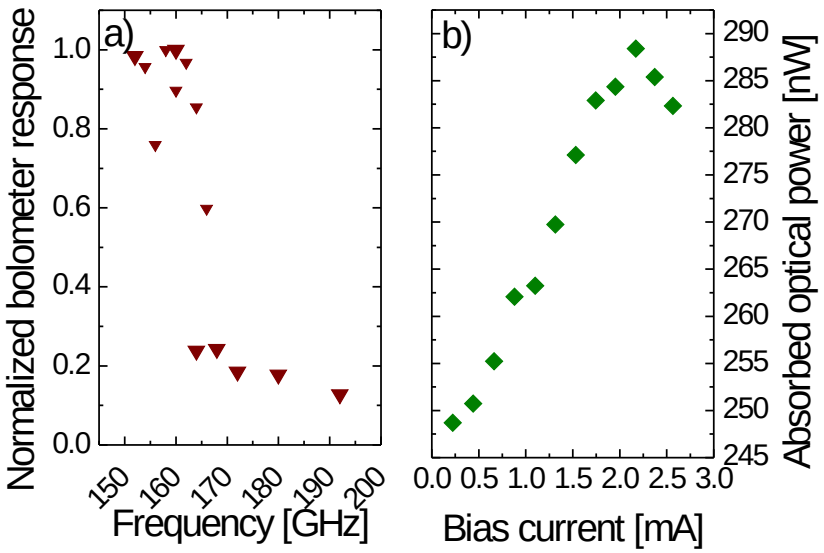

Figure 8: a) The optical response of the detector as a function of the RF frequency. b) The absorbed optical power, determined using the electrical responsivity from $P_{\mathrm{abs}} = V_{\mathrm{sig}}/S_{\mathrm{V}}(I)$. The maximum response corresponds to the bias where the bolometer resistance (207 Ω) matches the antenna input resistance.

was tuned to 155 GHz, and the signal amplitude was recorded while the bolometer bias current was increased. The electrical responsivity $S_{\mathrm{V}}(I)$ of the detector is known from the previous measurements. Figure 8 (b) shows the optical response of the device, normalized with the electrical reponsivity. An interesting feature is that the optical response peaks at about 2.1 mA, after which it reduces. The bolometer resistance at this bias was 207 Ω. We attribute the reducing optical response at larger currents to the increasing impedance mismatch between the bolometer and the antenna. We consider this as an interesting method of characterizing antenna input resistance with a direct measurement.

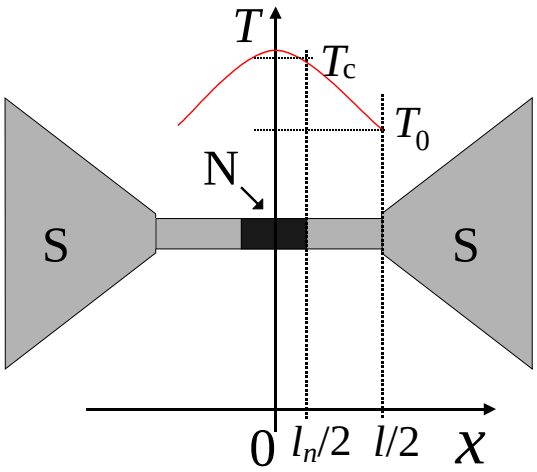

Figure 9: The hot-spot model for the Nb bridge.

3.2 Superconducting antenna-coupled microbolometers

As was shown in Section 2.1, cooling of bolometers improves their NEP significantly. Here we describe briefly the properties of superconducting hot-spot Nb bolometers, discussed in detail in Paper V. Superconductors, when operated at T_c are very sensitive thermometers making them an attractive choice for bolometer thermal sensing elements. Transition-edge microcalorimeters also utilize this property, and they shall be discussed in Section 4.

In order to make use of the large responsivity achievable with superconductors, one has to optimize the noise performance such that the Johnson noise and the thermal fluctuation noise are comparable, i.e. that the thermal isolation of the bolometer is sufficient. This can be achieved by removing the substrate from below the thermal sensing element, as was discussed above in Section 3.1. The bridge is voltage biased, which introduces negative electrothermal feedback which maintains a part of the bridge within T_c, while the bath temperature is maintained at 4.2 K. Such a bridge can be modeled with a simple hot-spot model [25, 26], where superconductivity enters the bridge from its ends, leaving a dissipative normal region to the centre portion of the bridge, as shown in Fig. 9. Incoming optical power P_{opt} modulates the size of the normal region and thus the current through it. The model assumes steady state behaviour, which is justified by the fact that any typical signal is much slower than the estimated 1 μs thermal time constant of the bridge which is based on the bridge volume and specific heat of Nb in the normal

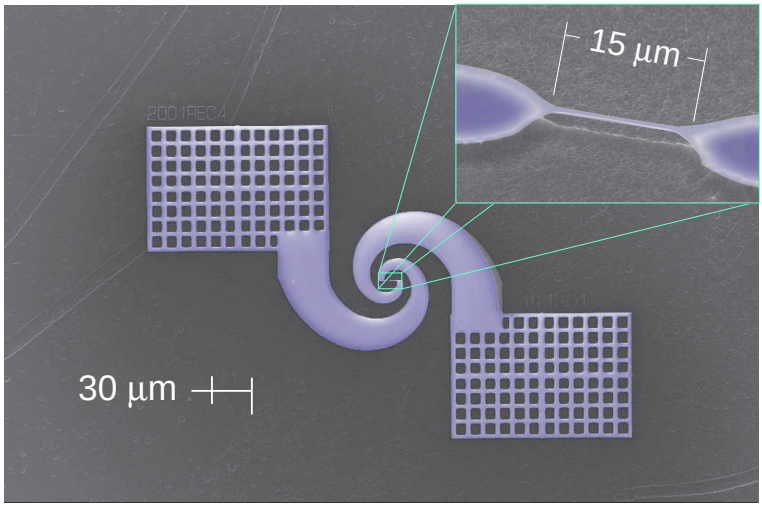

Figure 10: A SEM image of the Nb bridge bolometer, coupled to a logarithmic spiral antenna.

state. In the limit of small optical power, the solution for the $I(V)$ curve is

$$I(V)|_{P_{\rm opt}\to 0} = \frac{4\kappa(T_{\rm c}-T_0)}{Vl} + \frac{Vwt}{\rho_{\rm N} l}, \tag{31}$$

where κ is the thermal conductivity of the Nb, w, l, t are the width, length and the thickness of the bridge, respectively, and $\rho_{\rm N}$ is the normal state resistivity of Nb. Our model assumes that the thermal conductivity is a constant, as the lattice thermal conductivity of the Nb is significant at 4.2 K. Moreover, the electrical thermal conductivity is a non-monotonous function of temperature due to the fact that below $T_{\rm c}$ the thermal conductivity can actually *increase* somewhat in disordered metals due to reduced electron-phonon scattering [27]. Thus, as it difficult to determine the exact dependence of κ on T, it is taken as a constant. The measurements were carried out in an evacuated can immersed in liquid He. First, the critical temperature of the bridge was measured to be 6.8 K by measuring its resistance with a small bias current against the bath temperature. From this measurement we also obtained $\rho_{\rm N} = 56$ $\mu\Omega$cm. This is considerably higher than the tabulated value of 16 $\mu\Omega$cm for Nb. The high normal state resistivity is likely caused by high impurity content, which is supported also by the $T_{\rm c}$, as the tabulated value for the critical temperature of Nb is 9.1 K. Next, the bridge, shown in Fig. 10, was biased in parallel with a 1.2 Ω shunt resistor, and the current through the bridge was measured with a SQUID [28]. The $I(V)$ characteristics are shown in Fig. 12. The hot-spot model was fitted with the experimental data,

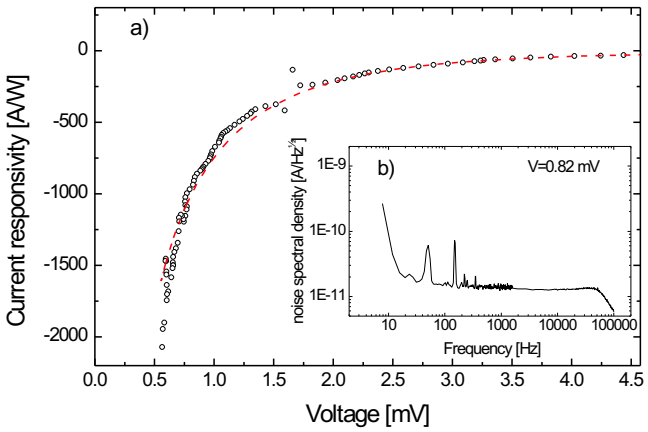

Figure 11: The electrical responsivity of the Nb bridge bolometer. The inset shows the current noise spectrum measured at $V = 0.82$ mV.

from which we obtained $\kappa = 0.54$ W/(Km), which is in agreement with the value predicted by the Wiedemann-Franz law [0.29 W/(Km)] and tabulated value for NbTi [0.28 W/(Km)] [29]. Using Eqs. (20) and (22), the current responsivity of the bridge can be calculated, shown in Fig. 11. Finally, the current noise spectra was measured at different bias points. A noise spectrum measured at $V = 0.82$ mV is shown in the inset.

The noise equivalent power of the bolometer is shown in Fig. 13. We note that the minimum NEP=14 fW/$\sqrt{\text{Hz}}$, which is almost an order of magnitude improvement over existing 4.2 K bolometers [8]. Our measurement was also limited by the noise of the SQUID, and better noise matching would enable a further improvement to NEP$\sim$ 3 fW/$\sqrt{\text{Hz}}$. Since the time constant is short, there exists the possibility of reducing G even further to improve the NEP. The increase in the NEP at bias voltages below 0.82 mV are due to electro-thermal oscillations which take place in the bias circuit when the effective time constant of the bolometer becomes comparable to the L_{SQUID}/R electrical time constant of the bias circuit [30],[V]. Thanks to the simple fabrication process, the device is scalable to large imaging arrays, and these arrays could be coupled to time or frequency multiplexed SQUID array read-outs, currently under intensive development for future 100 mK bolometer and microcalorimeter arrays [31, 32].

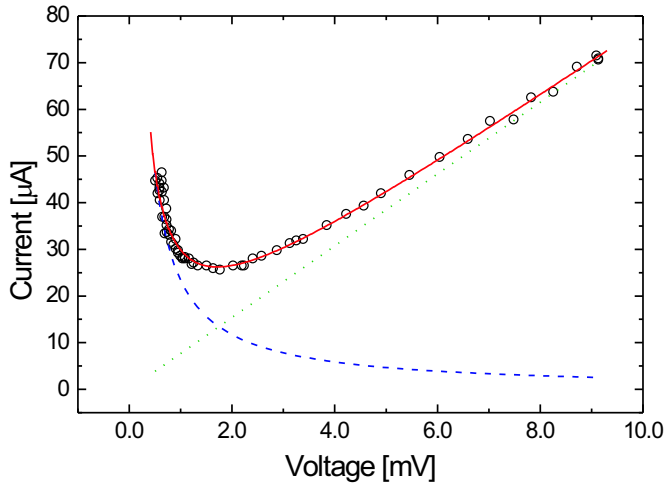

Figure 12: The $I(V)$ characteristics of the Nb bridge. The experimental data is represented by the circles, the solid line is the fit with $\kappa = 0.54$ W/(Km), the dotted line represents the Ohmic asymptote with the bridge in fully normal state, while the dashed line indicates the electro-thermal $\propto 1/V$ term. The smooth transition from ohmic to the partly superconducting region is smooth which is an indicative of a hot-spot type behaviour.

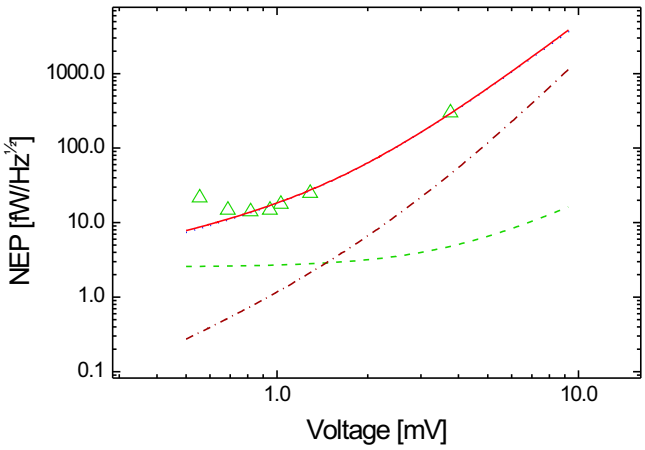

Figure 13: The electrical NEP of the Nb bridge bolometer. The experimental data are marked by triangles, while the the solid line represents the total modeled noise, consisting of contributions from the SQUID (dotted line, barely seen under the total noise), thermal fluctuation noise (dashed line), and Johnson noise (dash-dotted line).

4 Transition-edge microcalorimeters

When a transition from normal conductivity to superconductivity occurs in a thin film, a sharp drop to zero in the electrical resistance R of the film can be observed. Typical steepness of the transition $\alpha \equiv d\log R/d\log T$ is of the order of 1000, and thus the transition itself can be utilised as a very sensitive means of measuring changes in the temperature T of the film. This idea has been around for a long time [33, 34, 35], but experimenters had to use external feedback to maintain the operating point of the bolometer within the transition. Later, the idea of using voltage bias to provide internal negative feedback was introduced [36], and this, together with the existence of SQUID ammeters, made the breakthrough for practical transition-edge sensors (TESs).

When voltage bias is used, the superconducting film is maintained within the transition by the electro-thermal feedback, discussed in Section 2.1. As the film is first switched to the normal state by either an external magnetic field or by a large current exceeding the critical current, the bias point can be approached from the normal state by reducing the bias voltage. As transition is approached, current increases with decreasing voltage, since the bias power is maintained nearly constant, and thus $I(V) \approx P/V$ where P is given by the heat flow to the substrate at T_0, Eq. (12). It is interesting to note that had the bias source a truly zero impedance, the TES would switch to normal state with all finite V. In practice however, TES switches instead to the superconducting state at $V = \sqrt{R_\mathrm{s}P}$ as the resistance of the film becomes comparable to that of the internal resistance of the bias source R_s (the so called shunt resistance).

Typically, when biased with small current bias and when the $R(T)$ curve is measured by sweeping the bath temperature, α has a maximum value of about 300. When biased with a voltage bias, the situation is quite different, and in many cases α can be smaller by an order of magnitude. Now, the input joule power is much larger which has a two-fold effect on the transition: Firstly, the current flowing through the TES generates a magnetic field, which itself effects the critical temperature across the film. Critical temperature will tend to be suppressed at the edges of the film where the perpendicular component of the self field is at maximum. At the centre of the film, T_c is close to zero-field case. Secondly, there is a temperature gradient across the film due to dissipation and the effective value for α is obtained as an average over the temperature range in the film.

At this point it is relevant to discuss the magnetic properties of a TES film. The magnetic penetration depth of a titanium film is $\lambda = \sqrt{m_\mathrm{e}/\mu_0 n_\mathrm{e} e^2} \approx 30$ nm where m_e is the electron mass and $n_\mathrm{e} = 3.4 \cdot 10^{28}$

m^{-3} is the free electron density for Ti. The type of the superconductor can be determined from the ratio of the penetration depth to the coherence length, $\kappa = \lambda/\xi$. At T_c and in the dirty limit $\kappa = 0.715\lambda/\overline{l}$ where the mean free path is obtained from the normal state resistivity using

$$\overline{l} = \frac{(r_s/a_0)^2}{\rho_N} \times 92 \cdot 10^{-18}\ \Omega m^2, \tag{32}$$

with $r_s/a_0 = 2.1$ for Ti [37] where r_s is the radius of the conduction electron occupation volume and the Bohr radius $a_0 = 0.529$ Å. For a typical resistivity of $\rho_N = 3.81\ \mu\Omega$cm for our films, $\overline{l} \approx 110$Å. Thus, $\kappa \approx 2.7$ which suggests that the film is a type II superconductor. If there is a type I superconducting ground plane present, this will make the TES film also type I.

We can estimate the magnitude of the magnetic effect by comparing the critical current I_c with the typical operating current. The Ginzburg-Landau theory, combined with BCS critical field and penetration depth [30], yields a result for the critical current density $J_c = J_{c0}(1 - T/T_c)^{3/2}$ where

$$J_{c0} \approx 6.39(k_B T_c)^{3/2} \sqrt{\frac{N(0)}{\hbar \rho_N}} \approx 4\ \mathrm{GA/m^2}, \tag{33}$$

with $N(0) = 4.25 \cdot 10^{47}\ \mathrm{J^{-1}m^{-3}}$ is the density of states at Fermi surface for titanium [37]. For comparison, a typical current just before entering the transition is of the order 10 μA which corresponds to a current density ≈ 1 $\mathrm{MA/m^2}$ for a typical cross sectional area of 10 $(\mu\mathrm{m})^2$. The current over the range of operating points is typically below 50 μA. From the Bean's critical state model [38, 39], the current density distribution for a thin superconducting film is given by

$$\begin{aligned} J(x) &= \frac{2\pi J_c}{\pi} \arctan\left(\sqrt{\frac{w^2 - a^2}{a^2 - x^2}}\right) \quad |x| < a, \\ &= J_c, \quad a < |x| < w, \end{aligned} \tag{34}$$

where the majority of the current is carried at the edges where $J = J_c$ while the width of the field-free region is determined by the penetration depth $\lambda(T) = \lambda(0)/\sqrt{1 - (T/T_c)^4}$ and is given by $a = w\sqrt{1 - (I/I_c)^2}$. Figure 14 shows a finite-element calculation of the temperature and current distribution in a square TES using the critical state model.

4.1 X-ray measurements with a square TES

Initially, studies at our group focused on the development of square TES microcalorimeters based on titanium-gold proximity bilayers. Details of the

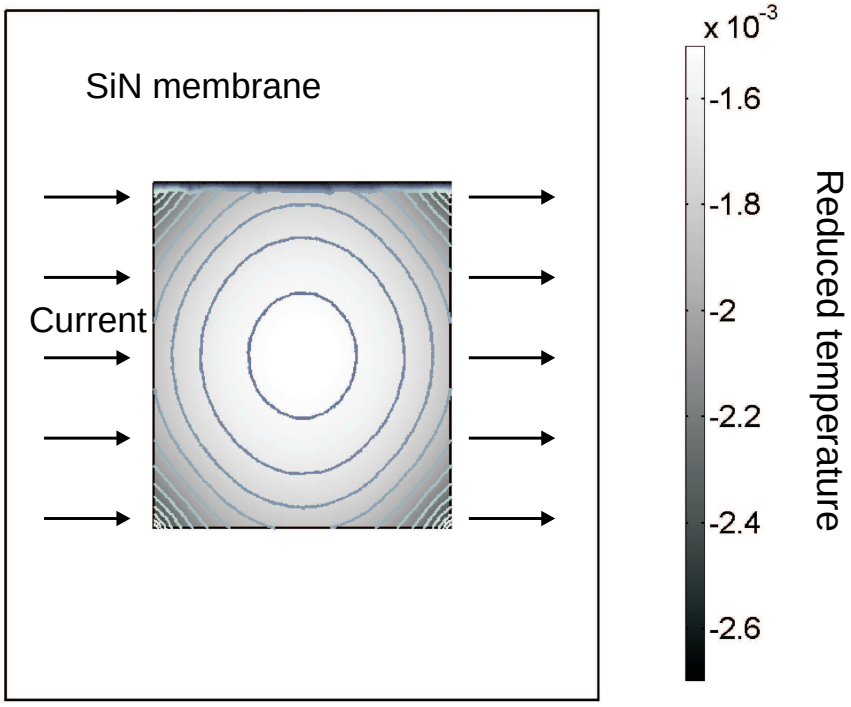

Figure 14: The temperature and current distribution across a 250 $(\mu\text{m})^2$ TES with a normal state resistance of 0.3 Ω, calculated using a 2-dimensional finite-element model. The temperature gradient in reduced temperature units is indicated by the levels of gray, while contours indicate the constant current density contrours. The bias voltage is 0.1 μV.

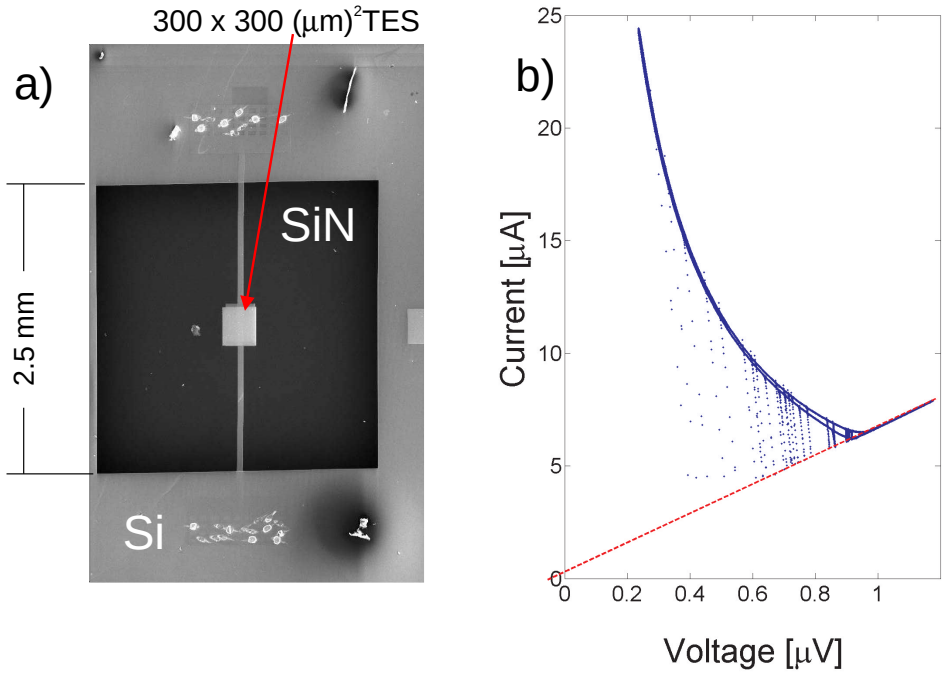

Figure 15: a) A SEM image of a square TES. The relevant dimensions are marked to the picture. The thickness of the SiN membrane was 250 nm. b) The $I(V)$ curve of a square TES. The spikes below 0.9 μV are due to X-ray events absorbed to the detector during the voltage sweep. The dashed line corresponds to the normal state resistance of 0.15 Ω. The X-ray energy drives the sensor close to the normal state.

fabrication procedures can be found from Ref. [40]. A SEM image of the 300 μm $\times$ 300 μm sensor is shown in Fig. 15 a). This device had a T_c = 150 mK and a normal state resistance of 150 mΩ. The measured $I(V)$ curve is shown in Fig. 15 b). The detector was biased in parallel with a 7 mΩ shunt resistor, and the current through the TES was measured with a SQUID with a current noise of 10 pA/$\sqrt{\text{Hz}}$. Bath temperature was maintained at $\approx$20 mK. The spikes in the curve are due to X-ray events absorbed during the measurement. The pulses almost touch the line extrapolated from the normal state, which implies that the photon energy is close to saturating the sensor.

Taking in to account the thermal fluctuation noise and Johnson noise in the TES, the full-width at half maximum (FWHM) energy resolution of a

transition-edge sensor X-ray microcalorimeter is given by [36]

$$\Delta E_{\mathrm{FWHM}} = 2.36\sqrt{k_{\mathrm{B}}T_{\mathrm{c}}^2 C}\,\xi_{\mathrm{etf}} \tag{35}$$

with

$$\xi_{\mathrm{etf}} = 2\left[\gamma\left(\frac{1}{\alpha\mathcal{L}_0}\right) + \left(\frac{1}{\alpha\mathcal{L}_0}\right)^2\right]^{1/4} \tag{36}$$

describing the effect of the electro-thermal feedback to the energy resolution of the sensor. If the detector noise is limited by the thermal fluctuation noise, $\xi_{\mathrm{etf}} < 1$. For the SiN thermal link used, $\gamma = 0.432$.

We can make a crude estimate of the energy resolution for the detector using Eq. (35) with parameters obtained in the measurements. We estimate the overall heat capacity of the sensor to be about 2.4 pJ/K. This number is obtained by calculating the contributions to the heat capacity from the 300 μm $\times$ 300 μm bismuth absorber on top of the TES, and the Ti/Au TES at 150 mK. The layer thicknesses were 3 μm for the Bi, 73 nm for the Au and 26 nm for the Ti. The heat capacity is given by $C = c_{\mathrm{V}}V$ for the layers with volume V, where $c_{\mathrm{V}} = \gamma_s\rho_m T_{\mathrm{c}}/(am_{\mathrm{a}}N_{\mathrm{A}})$ is the heat capacity per unit volume calculated using the molar specific heat γ_{s}, mass density ρ_{m} and atomic mass a for each material. N_{A} and m_{a} correspond to the Avogadro's constant ($N_{\mathrm{A}} = 6.022 \cdot 10^{23}$ mol^{-1}) and the atomic mass unit ($m_{\mathrm{a}} = 1.661 \cdot 10^{-27}$ kg), respectively. For the Ti layer, the heat capacity is multiplied by a factor 2.43 due to the increase in the specific heat at T_{c}. The bias dissipation at the operating range was 6 pW, which yields an average thermal conductivity $\overline{G} = P_{\mathrm{b}}/(T_{\mathrm{c}} - T_0) \approx 55$ pW/K. The dynamic thermal conductance G in terms of the average thermal conductivity is obtained from [41]

$$G = n\overline{G}\frac{1 - T_{\mathrm{c}}/T_0}{1 - T_{\mathrm{c}}^n/T_0^n}, \tag{37}$$

where $n \approx 3$ for SiN, and using the values for this sensor $G \approx 120$ pW/K, yielding an intrinsic time constant of $\tau_0 = 20$ ms. From measured pulses an effective fall time of 260 μs was obtained, which implies an average loop gain of $\overline{\mathcal{L}}_0 \approx \tau_0/\tau_{\mathrm{meas}} \approx 80$. Next, we estimate α by noting that the characteristic X-rays at energy $E = 5.89$ keV almost saturate the sensor, which can be seen from the $I(V)$ curve with X-rays almost reaching the line corresponding to the normal state resistivity, $\Delta T = E/C \approx 0.5$ mK $\approx 0.8\Delta T_{\mathrm{c}}$. Thus, $\alpha \approx T_{\mathrm{c}}/\Delta T_{\mathrm{c}} \approx 300$. Inserting the values to Eqs. (35) and (36), the resulting theoretical resolution is 12.7 eV $\cdot 0.13 = 1.7$ eV.

The measured X-ray spectrum is shown in Fig. 16. A fit calculated using a convolution of the gaussian detector response and the Lorenzian line shape

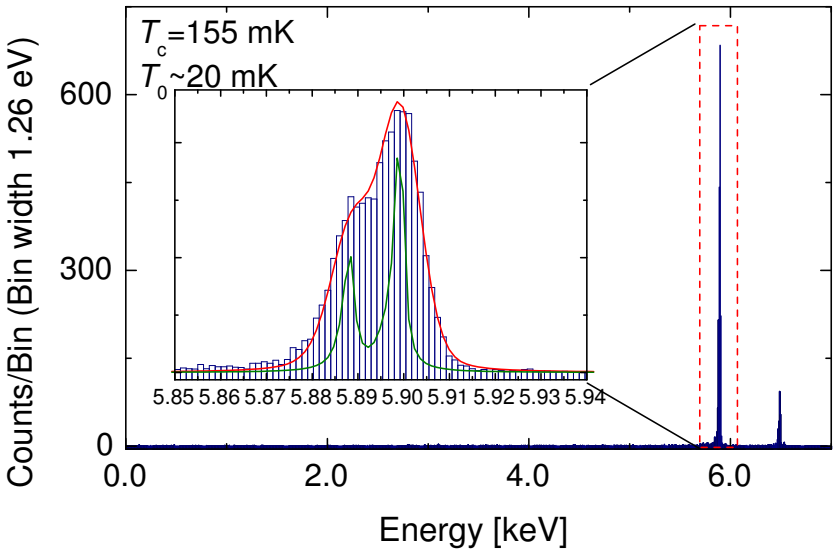

Figure 16: The Mn K-line spectrum measured with the square TES. The detector resolution is (9.1 ± 0.1) eV. The insert shows an expaned view of the K_α line.

for the Mn K_α complex yields a detector resolution of (9.1 ± 0.1) eV. Thus, the experimental value for $\xi_{\rm etf} = 0.72$. The possible explanations for the discrepancy are position dependent energy losses in the Bi absorber, non-optimum analogue filtering, or alternatively excess noise, either due to internal energy fluctuations [17], or noise due to fluctuation superconductivity, which shall be addressed in Section 5.

4.2 TES in Corbino disk geometry

Rectangular X-ray microcalorimeter TESs, such as the one described in Section 4.1, are rather vulnerable to imperfections and irregularities in the TES film. One common complication is imperfect contact between the superconductor and the normal metal [42] or different relative thicknesses for the two metals due to different wetting properties of the metals. In either case, the critical temperature at the edges is modified. In a typical situation, the $T_{\rm c}$ is higher at the edges, which effectively decreases the steepness of the transi-

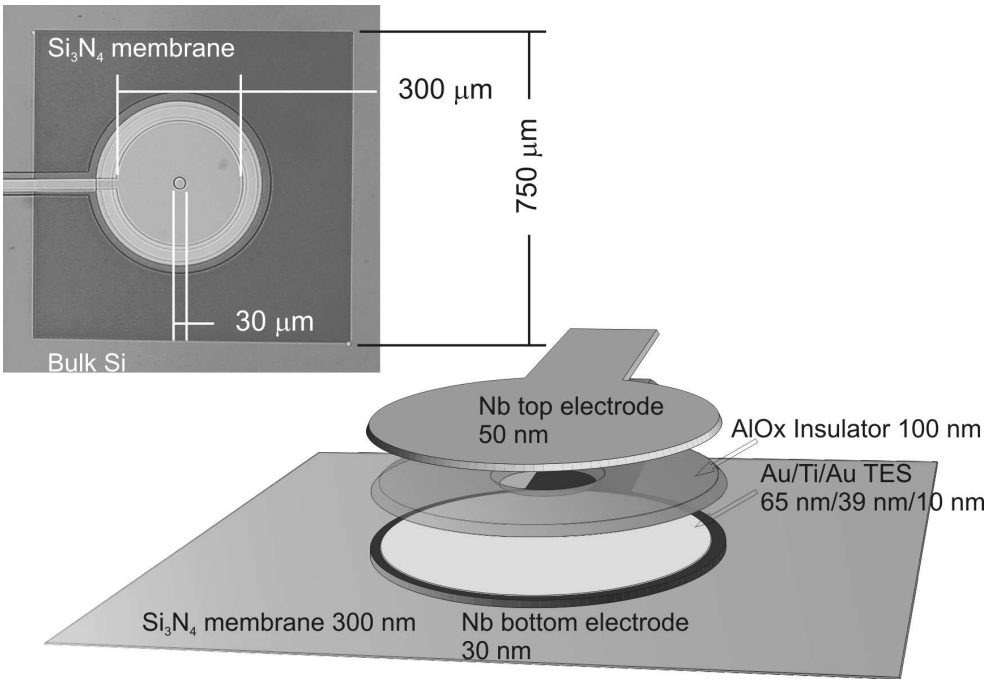

Figure 17: A diagram of the Corbino disk TES. The micrograph on top left shows the lateral dimensions of the device. Film order and typical thicknesses are shown in the exploded view of the CorTES.

tion. Moreover, the self-field, discussed briefly above, spreads the transition significantly when voltage biased. To counter these issues and eliminate the imperfections of the edges, we started investigating an edgeless geometry, the so-called Corbino disk [43]. A schematic of the geometry is shown in Fig. 17. In this geometry, the bias current is fed to a circular inner contact, and collected at an outer contact at the perimeter of the annular TES. Thus, the current distribution is radial. Thanks to the current distribution and the ground plane, the magnetic field near the film is azimuthal, has no radial dependence. The magnetic field, calculated from the vector potential, is shown in Fig. 18. Not only does this geometry eliminate uncontrollable phenomena at the edges of the film, but it also makes the analytical modeling of the TES simpler, as the current density is determined by the geometry. The Corbino disk TESs are processed on a double-side nitridized 525 μm thick $< 100 >$ silicon wafer. The low-stress Si_3N_4 is grown[2] by low pressure chemical vapour deposition (LPCVD) technique to a thickness of 250 nm.

[2]The nitride is processed at the Microfabrication Laboratory, University of California, Berkeley, USA.

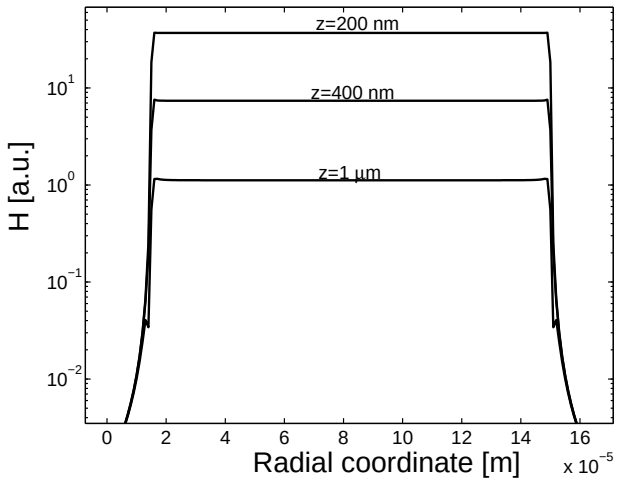

Figure 18: The magnetic field of the transport current as a function of the distance from the Corbino disk TES. The field is azimuthal, and constant over the film. The different curves correspond to different thicknesses of the insulator, located between the TES and the superconducting ground plane.

First, a rectangular opening is patterned to Si_3N_4 at the back side by the use of UV photolithography and reactive ion carbon tetrafluoride (CF_4) and oxygen (O_2) plasma etch (RIE). Next, an anisotropic KOH wet etch of the bulk Si takes place along the lattice boundaries, until a free-standing 750 μm $\times$ 750 μm nitride window is released.

Next, a double-layer polymer resist is spun on the wafer with thicknesses of about 300 nm - 400 nm for the two polymer layers. Patterning is done with electron-beam lithography (EBL). Although the feature size of the structures would allow the use of photolithography, we have decided to use EBL for its versatility and better lift-off properties. The first metal layer to be deposited is the bottom superconducting contact, which makes a contact to the TES at the circumference. The evaporation is done with a ultra-high vacuum (UHV) electron gun evaporator with a base pressure of about 10^{-8} mbar.

The niobium layer is deposited at a rate of 0.3 nm/s to a thickness of 50 nm, followed by a contacting layer of gold with a thickness of 10 nm. Next, a second set of EBL resists are spun, and the annular TES shape is patterned. Intially we had difficulties in controlling the critical temperatures of our TES films when using proximity bilayers, see Fig. 19. The Ti layer was deposited first, followed by the Au layer. This order was chosen due to adhesion, as Au tends to peel off the Si_3N_4 substrate. The problem arises as the Ti layer getters impurities while the Au target being changed in place,

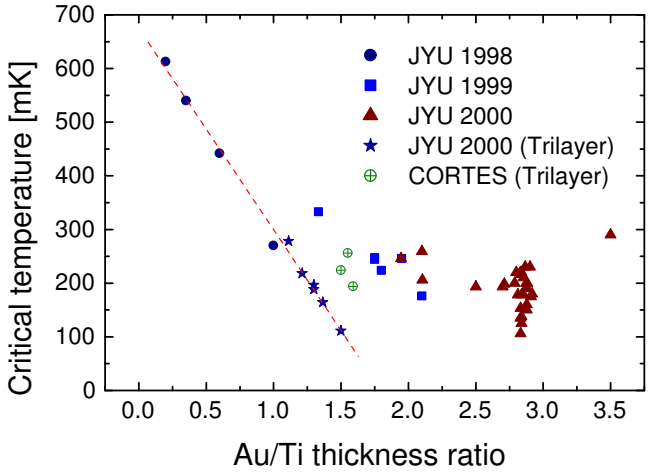

Figure 19: The dependence of T_c on the relative thicknesses of Au and Ti with a thickness in the range 50 nm - 200 nm. The results from 1998 were obtained after a new UHV evaporator was installed. The gradual contamination is clear from results from 1999, leading to the results of 2000 when the control of T_c become impossible. A trilayer -TES was then developed which avoided the contact contamination problems associated with bilayers. Also the fabrication of the CorTES proved to be difficult if the TES films were deposited on the AlOx insulator, a generous source of impurities. After we switched to evaporating the AlOx on the TES, the T_c become controllable again. The dashed line represents a fit $T_c = T_{c0} - md_{Au}/d_{ti}$ with $T_{c0} = 642$ mK and $m = -330$ mK.

and generates an impurity layer which prevents a good electron-transparent interface from forming with the gold as it is deposited. As a result, the critical temperatures measured seemed to saturate to about 200 mK, and increasing the Au thickness had little or no effect on the T_c. To counter the problem, we resorted to trilayers, where the superconducting Ti is sandwiched between two layers of Au. As passive Au is used as the first layer, the interface is clean for the Ti. The TES films are deposited with first a thin (10 nm) Ti adhesion layer, an Au layer of about 60 nm, followed by the Ti layer with a thickness of about 40 nm. The last layer is another Au layer (10 nm thick) which serves as a contacting layer for the other Nb layer.

In order to avoid short circuiting the TES with the superconducting Nb

top electrode, an insulating layer is required. We have experimented with silicon monoxide (SiO) and aluminium oxide (AlOx), of which the latter has proven to provide more reliable results. The insulator is evaporated after resist spin and EBL in a separate electron beam evaporator (base pressure $\sim 10^{-5}$ mbar). To avoid step coverage issues, the sample is mounted at a 10° angle and the sample mount is rotated at about 60 r/min while the AlOx is evaporated to a thickness of 100 nm at a rate of 0.1 nm/s.

Finally, the top electrode which serves as a superconducting ground plane and the centre contact is fabricated using EBL and UHV evaporation to a thickness of 40 nm. In addition, after deposition of the Au contacting layers, a short O_2 plasma etch is performed to clean the metal interface.

Characterization of the CorTES was carried out by first measuring the $R(T)$ curve with a small current bias. The superconducting transition of a Corbino-disk TES is shown in Fig. 20. This measurement was performed using an AC current bias (with a load impedance of 1 MΩ), and measuring the voltage across the TES using the lock-in technique while the bath temperature is swept across T_c. In this method the bias dissipation is very small ($\lesssim 1$ pW) and the TES film is maintained isothermal and at the same temperature as the substrate. Thus, Fig. 20 represents the intrinsic width of the superconducting transition which is mainly due to nonuniformities in the film.

Next, the critical current was measured by using a switching current measurement, where the device was cooled to 30 mK, and short 1 μs current pulses were injected with a 10 ppm duty-cycle to the device with increasing amplitude until a voltage pulse was detected across the CorTES. From the measurement, we obtained a critical current density of 36 MA/m^2. This discrepancy compared to the prediction given by Eq. (33) can be attributed to the Nb contacting layer. Further study of SEM images, for example Fig. 21, showed that the top Nb ground plane has problems covering the opening in the SiO. This is due to the formation of a SiO eave as the SiO is deposited at an angle. We fabricated test samples with Nb wires (100 μm × 744 nm × 150 nm) crossing a 100 nm thick layer of silicon monoxide. The switching current measurement yielded a critical current density of 20 MA/m^2, close to the value measured for the CorTES. Although the step coverage has proven to be problematic, TES operation is not compromised as long as the critical current of the wiring is larger than the maximum operating current given by $I_{\max} = \sqrt{P/R_s}$ which is typically about 30 μA.

The circular geometry allows for straightforward analytical modeling of the TES. If we assume radial symmetry, the current density is given by $J(r) = I/2\pi rd$, where r is the radial coordinate and d is the thickness of the TES. Approaching T_c from the normal state (which is the case when biasing

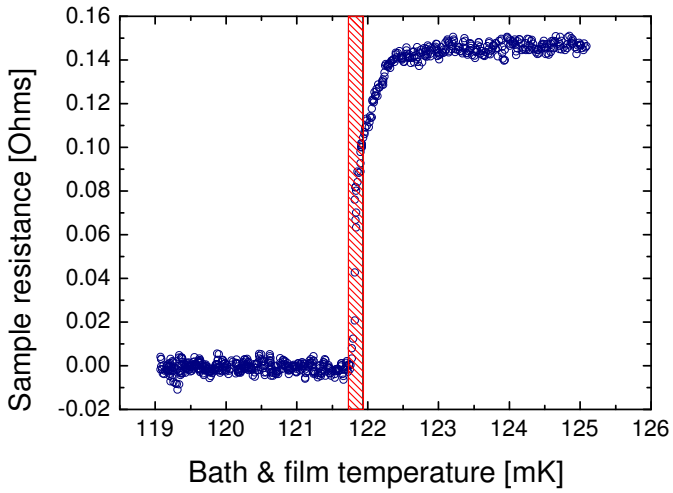

Figure 20: The constant-current superconducting transition of a Corbino disk TES. The striped region corresponds to a typical (200 μK) temperature gradient across the device when biased with voltage bias.

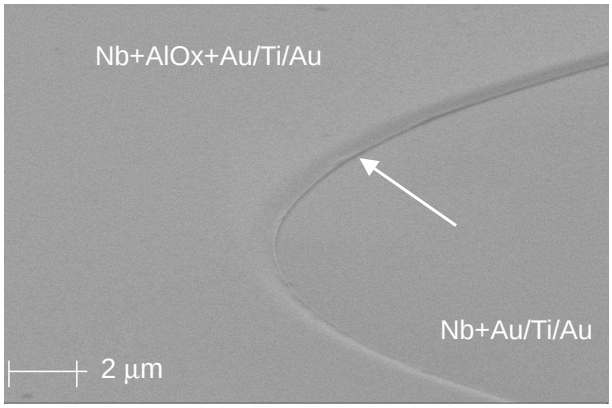

Figure 21: Step coverage with evaporated Nb is problematic due to the formation of a SiO eave (marked with an arrow) during the insulator deposition.

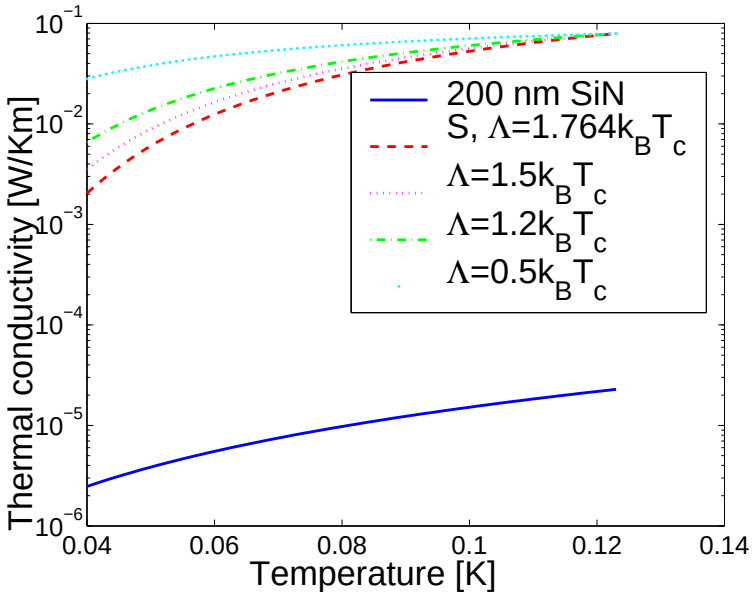

Figure 22: A comparison between the thermal conductivity of the supporting SiN membrane and the metal films on it. The solid line at the bottom is the thermal conductivity of a 200 nm thick SiN membrane. The various graphs at the top of the figure correspond to the thermal conducitivity of the TES films with various values of the parameter Λ.

TESs to the operating point), the edge of the CorTES at r_1 reaches T_c first, and thus superconductivity begins to fill the disk from the edge. Assuming that the resistivity is either zero or equals the normal state resistivity of the film, the resistance of the device is given by

$$R = \frac{\rho_N}{2\pi d} \ln \frac{r_b}{r_i}, \tag{38}$$

where ρ_N is the normal state resistivity of the TES film, d is the film thickness, r_i is the radius of the inner contact, and r_b is a time-averaged equilibrium normal-superconductor boundary.

We note that the thermal conductivity of a corbino disk TES is completely dominated by the heat transport in the metal films. From experimental results of Ref. [44], the thermal conductivity of the 250 nm thick silicon nitride membrane at around 100 mK is $\kappa_M = \mathcal{A}T^{\mathcal{B}}$ with $\mathcal{A} = 14.5 \cdot 10^{-3}$ W/(K$^{\mathcal{B}+1}$m) and $\mathcal{B} = 1.98$, whereas the thermal conductivity of the TES films at temperatures below T_c is given by

$$\kappa_S(T) \approx \kappa_N e^{-\Lambda/k_B(1/T-1/T_c)}, \tag{39}$$

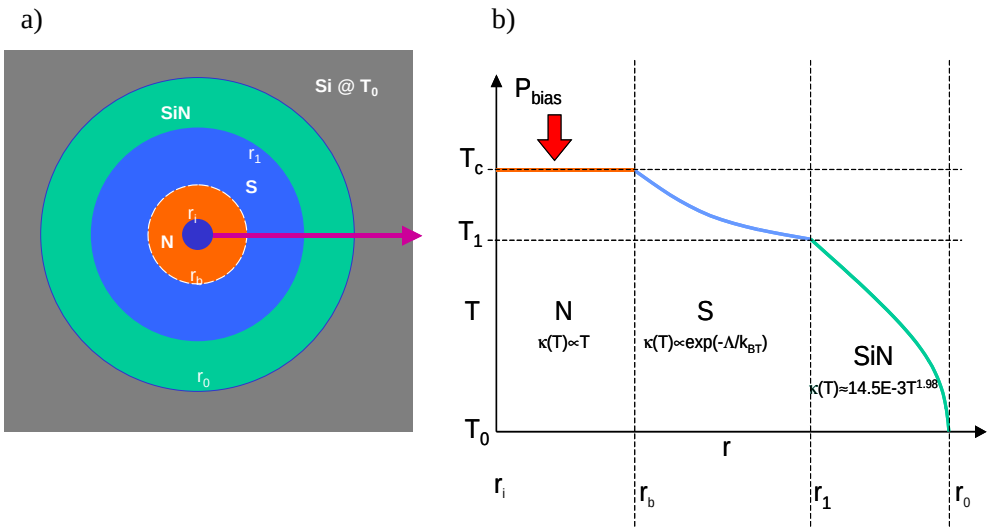

Figure 23: The thermal model of the CorTES. a) Different annular regions of the CorTES depicted in a top view. The innermost circle (radius r_i) is the superconducting central electrode, r_b is the radius of the equilibrium phase boundary. The superconducting region extends from r_b to r_1. The membrane is the region between r_1 and r_0. b) The temperature profile along the radial direction in the CorTES. The normal state part (N) is treated as isothermal. In the superconducting part (S) the thermal conductivity is assumed to take an exponential dependence on the temperature.

where $\kappa_\mathrm{N} = LT_\mathrm{c}/\rho$ is the thermal conductivity of the TES films in normal state as given by the Wiedemann-Franz law with $L = 2.45 \cdot 10^{-8}\mathrm{V}^2/\mathrm{K}^2$ the Lorentz number. The parameter Λ is of the order of the energy gap $\Delta \simeq 1.764 k_\mathrm{B} T_\mathrm{c}$ of the superconductor. A comparison between the thermal conductivities are shown in Fig. 22. As the film thicknesses are comparable ($d_\mathrm{TES} \approx 100$ nm), it is clear from the figure that the heat transport is dominated by the transport through the metal films. It is thus justified to simplify the thermal model so that the effect of the nitride below the TES films can be neglected.

Now, the thermal model is depicted in Fig. 23. At this point we assume that the annular normal state region ($r_\mathrm{i} < r < r_\mathrm{b}$) is isothermal with $T_\mathrm{N} = T_\mathrm{c}$.

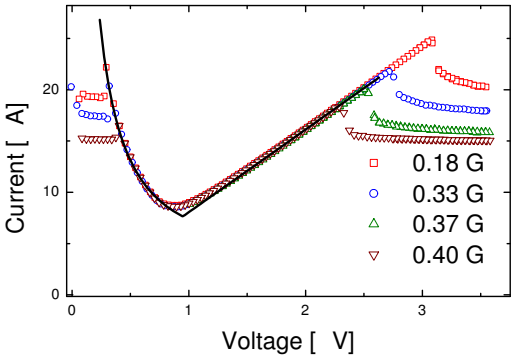

Figure 24: The $I(V)$ curve of the voltage-biased CorTES. Different values of external magnetic field were applied, and the low critical current of the wiring is evident. The $I(V)$ curve of the TES itself is not affected, as the external field is screened by the ground plane.

Equating the input bias power with the radial heat flux we obtain

$$\frac{\dot{Q}}{2\pi d}\int_{r_\mathrm{b}}^{r_1}\frac{1}{r}\,dr \;=\; -\int_{T_\mathrm{c}}^{T_1}\kappa_\mathrm{S}(T)\,dT \quad ,\mathrm{S-region}, \tag{40}$$

$$\frac{\dot{Q}}{2\pi d}\int_{r_1}^{r_0}\frac{1}{r}\,dr \;=\; -\int_{T_0}^{T_\mathrm{c}}\kappa_\mathrm{M}(T)\,dT \quad ,\mathrm{membrane} \tag{41}$$

where $\dot{Q} = V^2/R = V^2 2\pi d/\rho_\mathrm{N}\ln(r_\mathrm{b}/r_\mathrm{i})$ is the dissipated bias power and T_1 is the film temperature at the outer edge of the CorTES. The radius of the membrane r_0 is obtained by equating the circumference of a circular membrane with the circumference of a square one, $2\pi r_0 = 4w$, where w is the pitch of the square membrane. Eq. (41) gives a solution for T_1

$$T_1 = \left[\frac{V^2\ln\frac{r_0}{r_1}(\mathcal{B}+1)}{\rho_\mathrm{N}\ln\frac{r_\mathrm{b}}{r_\mathrm{i}}\mathcal{A}} + T_0^{\mathcal{B}+1}\right]^{\frac{1}{\mathcal{B}+1}}. \tag{42}$$

Inserting this to Eq. (40), carrying out the integration and then solving numerically for r_b, a solution for the $I(V)$ curve is obtained. The measured $I(V)$ curve at $T_0 \approx 10$ mK is compared with the a fit in Fig. 24. Fitting parameter is the parameter Λ, i.e. the thermal conductance of the superconducting film. Best fit yields $\Lambda = 1.25 k_\mathrm{B}T_\mathrm{c}$, a reasonable value as typically $k_\mathrm{B}T_\mathrm{c} < \Lambda < 2k_\mathrm{B}T_\mathrm{c}$ [27]. The simplified model assumes zero width for the

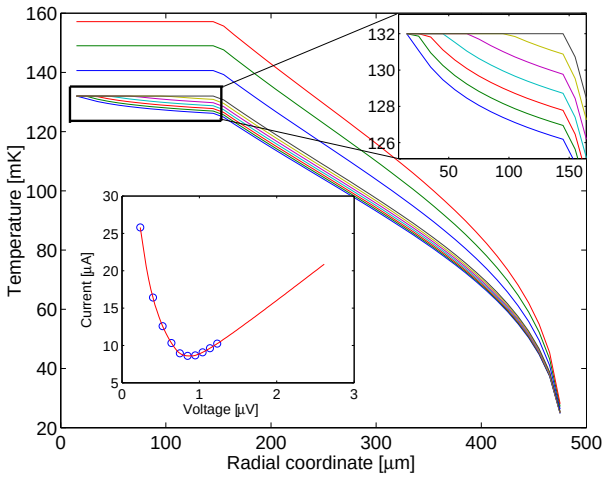

Figure 25: The temperature profile at various bias voltages, marked to the inset showing the measured $I(V)$ curve. The profile in the superconducting region is shown expanded at top right.

transition which produces the sharp corner at $V = 0.8$ μV. The calculated temperature profile for a CorTES with r_i=15 μm, r_1=150 μm, $r_0 = 477$ μm, $T_c = 132$ mK, $T_0 = 20$ mK and $\Lambda = 1.25$ is shown in Fig. 25.

5 Excess noise in transition-edge microcalorimeters

Many groups working on TESs have reported that the observed noise can not be accounted for by the combination of thermal fluctuation noise between the heat sink and the detector, Johnson noise and SQUID noise [45, 46, 47, 48, 49]. Some resolution degradation can be accounted for by taking in account position-dependent energy losses of the incident photons which broadens the width of the spectral lines [50]. To add to the significance of the problem, first reports concerning excess noise in the transition region are already from 1969 [51]. To date, no conclusive explanation has come forth to explain this effect. In some cases, internal energy fluctuations across the thermal resistance of the TES can generate additional thermal fluctuation noise, which can be modeled accurately [17, 18]. At this point it is interesting to point out that the very observation of this type of internal thermal fluctuation noise implies that there is a substantial variation in T_c or a temperature gradient present inside a TES. This can be justified by a simple argument by taking two

resistors with resistances R_1 and R_2, with heat capacities C_1 and C_2, and assuming that energy fluctuations of δE take place in between them. Now R_1 and R_2 can be identified with two regions of a TES, say the two halves of the device. We assume that the transition characteristics are identical, i.e. $R_1(T) = R_2(T)$. Since $\delta T_1 = \delta E/C_1 = -\delta T_2$, and thus $\delta R_1 = -\delta R_2$ the change in the total resistance vanishes. Observation of ITFN thus requires that either R_1 or R_2 is zero (below T_c), or that α is vastly different between R_1 and R_2, i.e. that there is significant variation in T_c or a temperature gradient, compared to the intrinsic transition width, across the device.

In all the cases where the performance is degraded by the increased noise arising from the detector, the excess noise current increases as the resistance of the TES is decreased. This is highly undesirable, as the detectors are preferably biased close to the bottom of the transition in order to keep the response time of the TES short while maximizing the temperature change that results to detector saturation. If operated close to the normal state, the loop gain is smaller and the corresponding effective time constant is longer.

It is well known that superconductivity can exist in a metal even *above* T_c [52, 53]. It has also been shown with the microscopic BCS theory that these fluctuations generate current noise when an applied electric field is present [54]. Our approach is based on the Ginzburg-Landau (GL) theory, valid close to T_c, and with some simplifications the calculation of fluctuation effects is easy.

In the phenomenological GL theory, the superconducting phase is described by the complex order parameter $\psi(\mathbf{r})$, and $|\psi(\mathbf{r})|^\mathbf{2}$ is attributed to the local density of superconducting electrons, n_s. In the following calculations we assume that $\psi(\mathbf{r})$ varies slowly across the film and thus $\psi(\mathbf{r}) = \psi$. The GL free energy F is minimized at and above T_c when $|\psi|^2 = n_\mathrm{s} = 0$. However, at and above T_c thermal fluctuations in the order parameter $\delta\psi$ take place and their probability is proportional to $e^{-\delta F/k_\mathrm{B}T}$ with $\delta F \sim k_\mathrm{B}T_\mathrm{c}$ the fluctuation in the free energy of the condensate. Thus, close to T_c these fluctuations are quite common in small volumes since $\delta F \propto \Omega$, where Ω is the volume associated with the fluctuations [55]. The coherence length determines the spatial extent of the fluctuations, given in the dirty limit by

$$\xi(T) = \frac{0.855\sqrt{\xi_0 \bar{l}}}{\sqrt{1 - \frac{T_\mathrm{c}}{T}}} \tag{43}$$

where ξ_0 is the BCS coherence length

$$\xi_0 = \frac{0.18\hbar v_\mathrm{F}}{k_\mathrm{B}T_\mathrm{c}}, \tag{44}$$

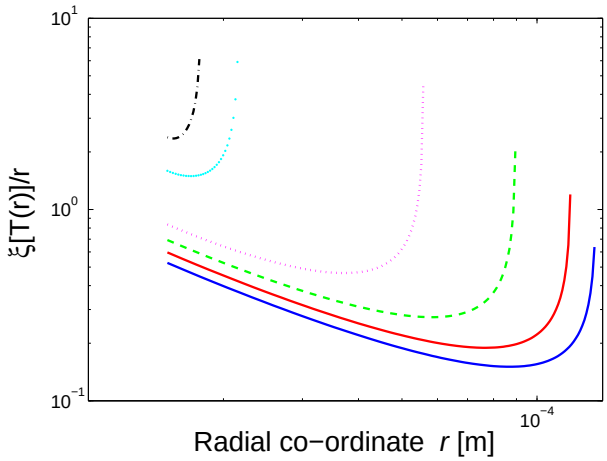

Figure 26: The normalized coherence length $\xi(T)/r$ plotted against the radial coordinate r at various different bias settings. At small bias ($V \lesssim 1$ μV) the fluctuations are fully correlated with $\xi(T)/r > 1$. The divergence corresponds to the location of the equilibrium phase boundary at each bias setting.

and $v_{\rm F} = 2{\cdot}10^6$ m/s is the Fermi velocity for Ti. Considering first the CorTES case (paper VI), we associate a fluctuation energy $\delta F \sim k_{\rm B}T_{\rm c}$ with a fluctuating volume $\delta\Omega$ within which the order parameter fluctuates between zero and $\delta\psi$, and calculate the corresponding displacement of the phase boundary δr. Due to the radial temperature gradient in the CorTES, the coherence length ξ diverges at the boundary, and the fluctuations are correlated. Figure 26 shows the coherence length plotted against the radial coordinate using the temperature distribution obtained from the fit to the $I(V)$ curve. Now

$$\delta F \simeq -\frac{\langle\alpha_{\rm GL}^2\rangle}{2\beta_{GL}}\delta\Omega = \frac{\alpha_0^2\langle T/T_{\rm c}-1\rangle^2}{2\beta_{\rm GL}}\delta\Omega, \tag{45}$$

where $\alpha_0 = 1.36\hbar/(4m_{\rm e}\xi_0\bar{l})$, $m_{\rm e}$ is the electron mass and $\beta_{\rm GL} = 0.108\alpha_0^2/[N(0)k_{\rm B}^2T_{\rm c}^2]$. Next, we approximate $\langle T/T_{\rm c}-1\rangle \simeq k\delta r$ where $k = T_{\rm c}^{-1}dT/dr|_{r=r_{\rm b}}$, and set the fluctuation in volume to $\delta\Omega = 2\pi dr_{\rm b}\delta r$, and solve for the displacement

$$\delta r = \left[\frac{0.108}{\pi dk^2 r_{\rm b}N(0)k_{\rm B}T_{\rm c}}\right]^{1/3}. \tag{46}$$

Deriving $T(r)$ in the normal region from the diffusion equation yields a result for the gradient at the boundary

$$k = -\frac{V^2}{T_{\rm c}^2 L r_{\rm b}\ln(r_{\rm b}/r_{\rm i})} \tag{47}$$

The spectral density of the phase boundary fluctuation is obtained by noting that the lifetime is given by (see, e.g. [55])

$$\tau_{\rm GL} = \frac{\pi\hbar}{8k_{\rm B}(T-T_{\rm c)}} \approx \frac{\pi\hbar}{8k_{\rm B}T_{\rm c}k\delta r} \tag{48}$$

and assuming that the fluctuation spectrum is white upto $\tau_{\rm GL}^{-1}$, the equivalent noise bandwidth is $\int_0^\infty (1+\omega^2\tau_{\rm GL}^2)^{-1}d\omega = \pi/(2\tau_{\rm GL})$. The noise spectral density of the resistance fluctuations is

$$\delta R_{\rm SD} = \frac{\rho_{\rm N}\delta r}{2\pi r_{\rm b} d}\sqrt{\frac{2\tau_{\rm GL}}{\pi}} = 0.12\rho_{\rm N}\left[\frac{\hbar^3}{\pi^7 N(0)k_{\rm B}^4 T_{\rm c}^4 r_{\rm b}^7 d^7 k^5}\right]^{1/6}, \tag{49}$$

and the resulting current noise is given by

$$\delta I_{\rm FSN} = \frac{dI}{dR}\delta R_{\rm SD} = \frac{I}{R}\delta R_{\rm SD}\frac{1+\beta}{2(1+\beta\mathcal{L}_0)}\frac{\sqrt{1+\omega^2\tau_0^2}}{\sqrt{1+\omega^2\tau_{\rm eff}^2}}. \tag{50}$$

A comparison between the model and the measured rms noise is shown in Fig. 27. The measurement was carried out at a bath temperature of 20 mK and the rms noise was measured in a frequency band from 100 Hz to 20 kHz as a function of bias voltage. The modeled noise includes contributions from the thermal fluctuation noise (TFN), the Johnson noise (JN), SQUID noise (SQN), internal thermal fluctuation noise (ITFN), and the fluctuation superconductivity noise (FSN). We used the Lorentz number as a fitting parameter, and a good agreement was obtained with $0.1L$. The physical explanation of this reduced Lorentz number is likely the fact that the Wiedemann-Franz law is not obeyed when the film is near $T_{\rm c}$, or alternatively simply due to the crude definition of our model. Also the noise spectra at various bias points were measured. Figure 28 shows the measured spectra together with fits with the model, and its components.

The discussion above assumed that the fluctuations correlate within a annular volume $2\pi r_{\rm b} d\delta r$. It is possible that the fluctuations correlate within the entire disk [56]. In this case the fluctuations can be calculated by first noting that

$$\frac{\delta^2 F}{\delta\psi^2}(\delta\psi^2) \approx \alpha_0\Omega k\xi_{\rm eff}(\delta\psi^2) \approx k_{\rm B}T_{\rm c}, \tag{51}$$

where $\xi_{\rm eff} = \xi_0/(k\xi_0)^{1/3}$ is an effective coherence length in the presence of the temperature gradient and Ω is the volume of the entire TES. The displacement of the phase boundary can be calculated by noting that $\langle|\delta\psi|^2\rangle =$

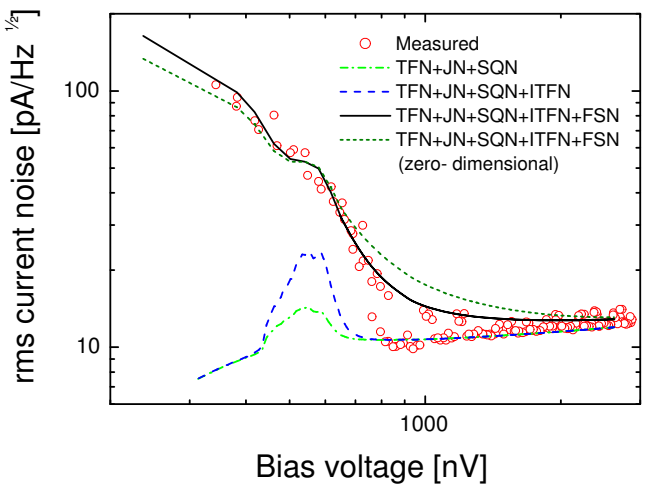

Figure 27: The measured rms current noise between 100 Hz and 20 kHz, marked by circles. The modeled noise, including the fluctuation superconductivity noise is marked by the solid line in the partly correlated case, and by the dotted line in the zero- dimensional case. The irregularities in the modeled curve are due to the fact that measured values for the voltage were used in the calculation of the noise. The dashed and dash-dotted lines represents the modeled data in absence of FSN, and shows the effect of internal thermal fluctuation noise (ITFN), which peaks at the voltage where α is at maximum.

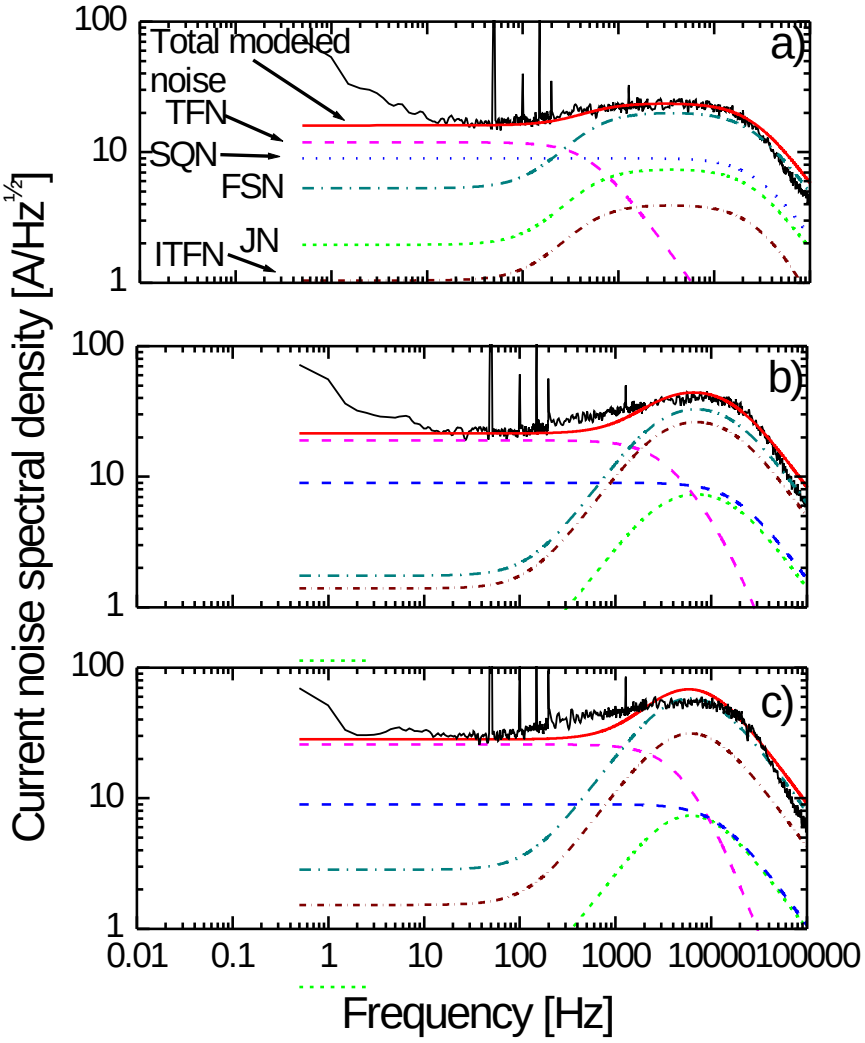

Figure 28: The noise spectra of the CorTES, measured at bias voltages of a) 0.75 μV, b) 0.62 μV, and c) 0.5 μV. The different contributions of thermal fluctuation noise (TFN), Johnson noise (JN), SQUID noise (SQN), internal thermal fluctuation noise (ITFN), and fluctuation superconductivity noise (FSN) are identified in the top graph.

$|d\psi/dx|^2\langle|\delta x_0|^2\rangle \sim (\psi_0/\xi_{\rm eff})^2\langle|\delta x_0|^2\rangle$. Using this result and Eq. (51), the fluctuation in the boundary radius is

$$\delta r \approx \sqrt{\frac{0.108}{N(0)k_{\rm B}T_{\rm c}\pi r_1^2 dk^2}}. \tag{52}$$

In this zero-dimensional case, the resistance fluctuations give

$$\delta R_{\rm SD0} = 0.1\rho_{\rm N}\left[\frac{\hbar^2}{N(0)k_{\rm B}^3T_{\rm c}^3\pi^3 r_1^2 d^5 k^4}\right]^{1/4}. \tag{53}$$

We note that the zero-dimensional case does not differ substantially from the partly correlated case. The zero- dimensional result is shown also in Fig. 27, and a good fit is in this case obtained with $0.5L$.

Next, we shall discuss shortly the possibility to optimize this noise in TES detectors. When approaching perfect voltage bias ($\beta \to 0$), the current noise becomes $\delta I = I\delta R_{\rm SD}/R$. Taking the terms in highest powers out of the square brackets in Eq. (49), noting that in Eq. (47) $\ln(r_{\rm b}/r_{\rm i}) = 2\pi Rd/\rho_N$ and approximating $r_{\rm b} \approx r_{\rm i}(1 + 2\pi Rd/\rho_N)$ the noise can be written as

$$\delta I_{\rm FSN}(0) = \frac{0.24IT_{\rm c}L}{V^2(1+\mathcal{L}_0)}\left[\frac{\hbar^3 T_{\rm c}^2 k}{\pi N(0)k_{\rm B}^4 dr_{\rm i}(1+2\pi Rd\rho_N^{-1})}\right]^{1/6} \equiv \frac{0.24IT_{\rm c}L}{V^2(1+\mathcal{L}_0)}\Gamma. \tag{54}$$

Now the term in the square brackets denoted by Γ can be considered a constant as it depends weakly on the parameters due to the 6th root. Remarkable is that very little is left to be optimized! In terms of NEP, the FSN contribution is given by

$$\mathrm{NEP}_{\rm FSN} = \frac{\delta I_{\rm FSN}}{S_{\rm I}} = \frac{0.24LT_{\rm c}}{R\mathcal{L}_0}\Gamma\sqrt{1+\omega^2\tau_0^2} = \frac{0.24LT_{\rm c}^2 G}{V^2\alpha}\sqrt{1+\omega^2\tau_0^2}, \tag{55}$$

i.e. that at low bias voltages this noise term will dominate over the other noise contributions. The value of Γ is between $1.0\cdot10^{-8}$ K/$\sqrt{\rm Hz}$ and $1.4\cdot10^{-8}$ K/$\sqrt{\rm Hz}$ over the operating range in our CorTES. If the FSN term dominates over the other noise sources, the energy resolution is [57]

$$\Delta E_{\rm FWHM} = 2.36\left(\int_0^\infty \frac{4df}{\mathrm{NEP}_{\rm FSN}^2}\right)^{-1/2} \approx 0.4\frac{LT_{\rm c}^2 G}{V^2\alpha}\Gamma\sqrt{\tau_0} \tag{56}$$

This implies that the NEP contribution of FSN in transition-edge sensors could be decreased if the normal state resistance is increased. However, one should be careful with this since it also increases the amplitude of the

internal thermal fluctuation noise, and is a potential problem in terms of noise matching to the SQUID.

To address the situation in a square TES sensor, similar treatment can be applied with simplifying assumptions, mainly that the current distribution is homogeneous and that we can treat the problem as one dimensional. We now assume that the dissipative region in a square TES is a rectangular region across the device with length $l_{\rm n} = Rwd/\rho_N$ where w is the width of the film. The solution for the temperature gradient in the normal region with boundary conditions $T(\pm l_{\rm n/2}) = T_{\rm c}$ and $T'(0) = 0$ is

$$T(x) = \frac{1}{2}\left(\frac{V^2}{L} + 4T_{\rm c} - \frac{4V^2 x}{L l_{\rm n}}\right)^{1/2}, \tag{57}$$

from which the equivalent of Eq. (47) is $k_\square = -V^2\rho_{\rm N}/(RwdLT_{\rm c}^2) = -P_{\rm b}\rho_{\rm N}/(2wdLT_{\rm c}^2)$ where we have used notation '$\square$' to make a distinction to the square geometry. Now

$$\delta I_{\rm FSN,\square} = 0.72\frac{IT_{\rm c}L}{V^2(1+\mathcal{L}_0)}\Gamma_\square, \tag{58}$$

where $\Gamma_\square = [\hbar^3 k_\square T_{\rm c}^2/(N(0)k_{\rm B}^4 wd)]^{1/6}$. Using typical parameters we obtain $\Gamma_\square \approx 1{\cdot}10^{-8}$ K/$\sqrt{\rm Hz}$, and the expression for NEP is as in Eq. (55). Although the treatment is somewhat oversimplified, Eq. (58) might be useful when predicting the excess noise in square TESs.

The fluctuation superconductivity noise contribution is larger in the CorTES geometry due to the fact that k increases faster towards the centre of the disk as the current density increases. A homogeneous current distribution thus seems a favourable choice. In addition, the CorTES is particularly vulnerable to FSN as the fluctuations are completely correlated. There remains a weak dependence on the temperature gradient, $k^{1/6}$, which might explain the fact that some groups see decreased excess noise when the TES is equipped with thick normal metal bars on the edges, or a thick Cu absorber in the centre, which effectively flatten out the temperature gradient across the device. Moreover, the normal metal acts as a constant parallel resistance with the TES film, which reduces the amplitude of the resistance fluctuations. This naturally decreases also the responsivity of the TES, but might allow the optimisation of the fluctuation superconductivity noise. Another possibility to reduce the excess noise is by simply dividing a TES to n parallel TESs, since in this case the FSN decreases as $n^{-1/3}$ since $\delta r \propto n^{1/6}$ and while $\delta R_{\rm SD} \propto n^{-1/2}$. In order to reduce FSN to the level of the thermal fluctuation noise,

$$n = \left(\frac{0.72T_{\rm c}^2 GL\Gamma}{V^2\alpha{\rm NEP}_{\rm TFN}}\right)^3 \tag{59}$$

6 On-chip cooling of microcalorimeters

Cooling of detectors to temperatures below 100 mK is by all measures a challenging task. Especially instruments which have limited room available and constraints regarding their operational lifetime, such as space-borne instrumentation, pose a significant technological challenge in terms of their cryogenic systems. The refrigerators in use today involve complicated liquid or gas handling systems and large amounts of liquid refrigerants. The most common cooling methods used well below 1 K are based either on the enthalpy of mixing of ^{3}He and ^{4}He or adiabatic demagnetization of paramagnetic salts, or nuclei in metals.

In this Section we present the results obtained with a solid state cooler where the effect is based on the evaporation of hot electrons of a metal. The device consists of a pair of normal metal - insulator - superconductor (NIS) tunnel junctions, where the hot electrons of the normal metal are removed by placing a voltage across the junctions which results to the tunnelling of the hottest electrons to the superconductor. This device is suitable for on-chip cooling of thermal detectors where the dissipation is of the order of picowatts.

The cooling effect in a NIS tunnel junction is based on the excistence of an energy gap $\Delta = 1.76 k_{\rm B} T_{\rm c}$ in the superconductor. Biasing the normal side at a voltage $V \lesssim \Delta/e$ the hottest electrons with an energy E above the Fermi level $E_{\rm F}$ can tunnel through the tunnel barrier to the superconducting side. As each electron carries out heat $E - eV$, the metal cools [58, 59, 60, 61]. A combination of two sets of junctions leads to a SINIS structure, and the net cooling power is doubled as the cooling is symmetric: On the opposite junction, quasiparticles with energy below $E_{\rm F}$, i.e. 'cool' quasiparticles tunnel to the normal metal. The net cooling power is obtained by integrating the energy driven through the junction resistance $R_{\rm T}$ over all the states in the electrodes

$$\dot{Q}_{\rm c} = \frac{1}{e^2 R_{\rm T}} \int_{-\infty}^{\infty} g_{\rm S}(E)[f(E - eV, T_{\rm N}) - f(E, T_{\rm S})](E - eV)\, dE, \qquad (60)$$

where $g_{\rm S}(E) = g_{\rm N}(0){\rm Re}[E(E^2 - \Delta^2)^{-1/2}]$ is the density of states in the superconductor, and $f(E,T) = \{1 + \exp[(E-\mu)/k_{\rm B}T]\}^{-1}$ is the Fermi-Dirac distribution at T and $\mu \sim E_{\rm F}$. Subscripts N and S refer to the normal metal and the superconductor, respectively. The maximum cooling power is reached when $V \lesssim \Delta/e$ [59, 60] when

$$\dot{Q}_{\rm cmax} \approx 0.6 \frac{\sqrt{\Delta}}{e^2 R_{\rm T}} (k_{\rm B} T_{\rm N})^{3/2}. \qquad (61)$$

The minimum achievable electron temperature in the normal metal is determined by the heat flow from the electron system of the normal metal to the

phonon system, given by

$$T_{\mathrm{Nmin}} = \left(T_0^5 - \frac{\dot{Q}_{\mathrm{cmax}}}{\Sigma\Omega} \right)^{1/5}, \tag{62}$$

where $\Sigma \sim \cdot 10^9$ $\mathrm{WK^{-5}m^{-3}}$ is a material dependent constant and Ω is the volume of the normal metal. A SINIS cooler can also be used to reduce the lattice temperature. This can be achieved by extending the normal electrode as a cold finger to a thermally isolated platform. Lattice refrigeration is desirable when cooling thermal detectors, as will be shown in Section 6.3.

6.1 Coolers with large junction area

The experimental results described in paper II were obtained with small area junctions which were fabricated on nitridized silicon wafers using EBL and thin film shadow mask deposition. The superconductor was a 15 nm thick layer of aluminium, which was oxidized in pure oxygen atmosphere prior to the deposition of the 20 nm thick copper normal metal. This masking technique allows fabrication of good quality junctions with a fairly small junction area of ~ 1 $\mu\mathrm{m}^2$ and below. The junction quality sets a lower limit for the junction barrier thickness: leakage currents degrade the cooling performance significantly in aluminium oxide junctions with a specific resistance (resistance $\times$ junction area) below 0.1 $\mathrm{k\Omega\mu m^2}$. Thus, in order to decrease R_{T} one has to fabricate junctions with larger area. With the EBL and shadow masking technique this is possible only by connecting several small junctions in parallel. A more desirable route is to increase the area of single junctions, as the parallel junction coolers tend to have excessive volume which increases the heat flow to the electron system from the phonons. This strategy was pursued in the work described in the first half of paper IV. In these experiments, the double-layer electron resist was replaced by a micromachined shadow mask, which was fabricated using photolithography, anisotropic wet etching of Si, and reactive ion etching. The use of this type of mask enabled us to increase the junction area significantly, up to 100 $(\mu\mathrm{m})^2$. However, with the large junction coolers it became evident that the thermalization of the superconductors becomes a crucial issue: the large tunnelling current from these junctions leads to an excessive population of quasiparticles near the junctions which have a finite probability of back-tunnelling to the normal metal, decreasing the cooling power drastically. The problem is circumvented by the use of so-called quasiparticle 'traps' [62]. The traps can be of high conductivity normal metal, placed in the vicinity of the junctions, whereby they transport the excess heat away from the junction area.

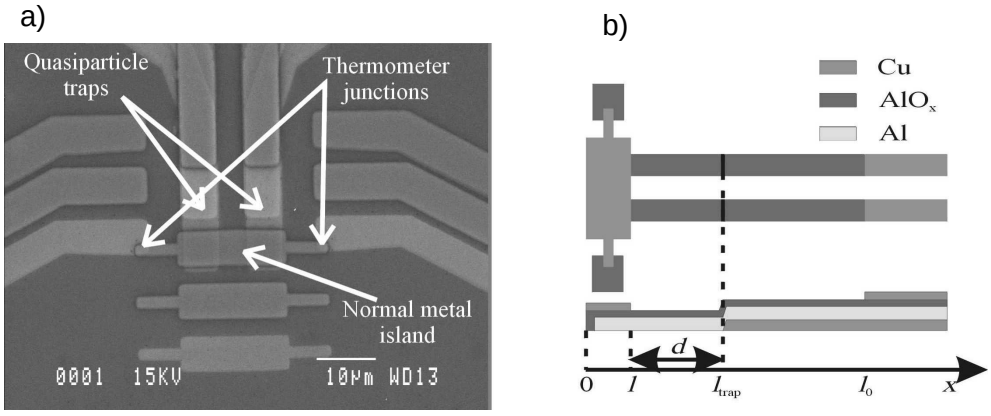

Figure 29: a) A SEM image of an electron cooler with large junctions. Also the Cu quasiparticle 'traps' are indicated with arrows. The two bars at the bottom of the figure are due to the shadows from the angle evaporation and do not affect the performance of the cooler. b) A side view of the structure showing the layer order.

6.2 Results from electron coolers

An electron cooler with 30 (μm^2) junctions is shown in Fig. 29 a). Also shown in the figure are the normal metal traps in close vicinity of the junctions, while a pair of small junctions are used for thermometry. A side view showing the layer order is shown in Fig. 29 b). Although having the traps displaced in the plane from the junctions gave satisfactory results, the control of the distance was difficult due to the required accuracy required in the evaporation angle of the traps. A slight misalignment can short the junction, thus removing the cooling effect. The outcome of the investigations on the optimum junction geometry and trap location indicated clearly that having the trap directly underneath the junction should provide the best cooling results. The next task was to overcome the difficulties of having the thick normal metal in contact with the Al, i.e. interdiffusion of the metals and proximity effect of the Cu on the Al. As a first trial, we tried depositing a thin ($<$ 10 nm) titanium layer in between the Al and the Cu trap as a diffusion barrier. In low temperature measurements, no cooling was observed. Since no additional trials were carried out, we are not sure whether the cooler failure was caused by the Ti or having something else being wrong with the cooler. According to our analysis, a very thin oxide layer could be transparent enough for the quasiparticles, while acting as a diffusion barrier for the metals. Also, the high probability of pin-holes through the thin oxide could

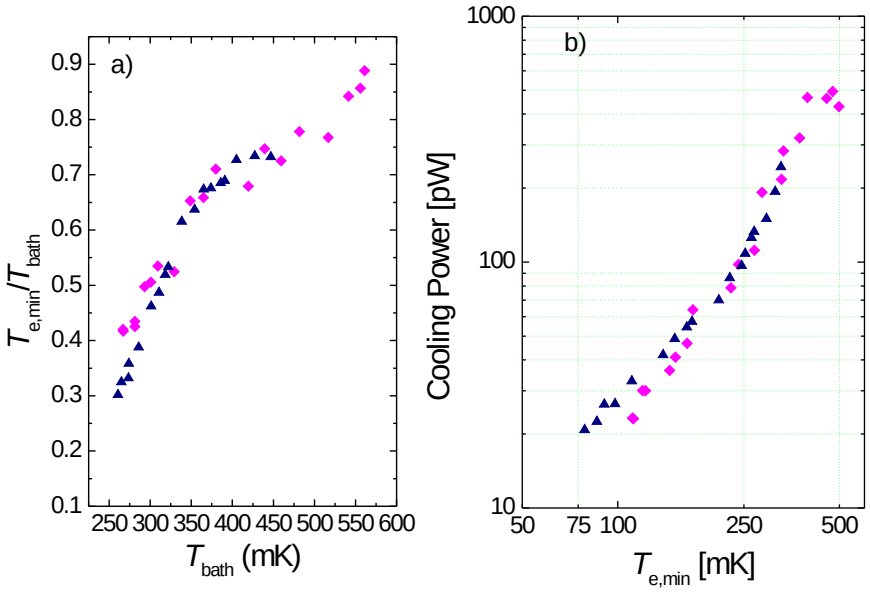

Figure 30: The best cooling results obtained with the electron coolers. a) The minimum electron temperature vs. the bath temperature, and b) the cooling power of the refrigerator.

actually be beneficial for the trapping process. Sandwiched coolers with a 5 nm thick AlOx between the superconducting Al electrode and the Cu trap were fabricated. A SEM micrograph of one device and the obtained cooling results from two devices are shown in Fig. 30. The trap appears to perform very well to the very lowest temperatures (80 mK), since no heating is seen in the cooling curves. Also, the cooling power, shown in the inset of the cooling curves is ∼20 pW at 80 mK, which is sufficient for most calorimeter applications.

6.3 Lattice coolers

In optimised thermal detectors (such as bolometers and calorimeters), the performance is limited by the random exchange of energy between the detector and its heat sink. This fluctuation is usually called 'phonon noise', and can be reduced by increasing the thermal isolation of the detector, or by cooling the device. We have shown in paper III that one must cool both, the detector *and* the heat sink in order to improve the sensitivity significantly. This is due to the fact that the phonon noise is in the non-equilibrium case proportional to $(T^{n+1} + T_0^{n+1})^{1/2}$, where n is either 4 or 5 depending on the limiting thermal conductance in the system [63].

Thus, in order to improve detector performance substantially with the SINIS, the actual heat sink of the device needs to be the cooled object. The natural way to start working towards this is to cool a thermally isolated platform, instead than just the electron gas in a metal. To do this, the normal metal island can be extended as a cold finger across a thermally well isolated bridge.

With the existing quality of materials, i.e. with non-superconducting metal elements in this case, the choice of the geometry of the cold finger extending between the heat bath and the membrane is a compromise. This arises from the competing effects of increased thermal conduction along the cold finger, when the cross sectional area is increased, and from the simultaneous decrease of thermal isolation due to the increased volume, and this way increased electron phonon heat transport in the cold finger on the substrate, outside the membrane. Typically we use copper, electron-gun evaporated in UHV ($<10^{-8}$ mbar), as the normal metal. RRR measurements of Cu films have been performed. The results are collected in Table 4. In thick (200 nm) films, an RRR of about 10 can be achieved, resulting in a substantial improvement in thermal conductance of the cold finger as compared to that of 10 times thinner films with five times lower resistivity ratios.

We get important limitations for the structure and geometry of possible SINIS refrigerators already from rather simple considerations. For exam-

	$w = 0.2$ μm		$w = 1$ μm		$w = 10$ μm	
	ρ(300 K)	RRR	ρ(300 K)	RRR	ρ(300 K)	RRR
$d = 30$ nm	2.9	1.9	3.2	2.1	3.3	2.2
$d = 75$ nm	2.2	2.7	2.2	3.4	2.3	3.8
$d = 300$ nm	1.8	5.3	1.8	8.7	1.7	10.3

Table 4: Resistivity ρ at 300 K (in $\mu\Omega$ cm) and RRR for Cu films with different thicknesses d and widths w. The tabulated value for bulk Cu is $\rho(300\text{K}) = 1.67$ $\mu\Omega$cm.

ple, the maximum thickness, d, of the normal-metal layer above the tunnel junction is determined by the competition between the cooling power and electron-phonon coupling. The maximum cooling power of a single junction with resistance R_T is given by Eq. 61 which is reached when V is slightly below Δ/e. Requiring that the electron-phonon heat flow in the junction area A, $\dot{Q}_{e-p} = \Sigma\Omega(T_{p,n}^5 - T_{e,n}^5)$, must be smaller than $\dot{Q}_\text{cmax}$, we get using the equation for $\dot{Q}_{e-p}$ and Eq. (61)

$$d < \frac{0.6\sqrt{\Delta}}{e^2\Sigma}\frac{1}{R_\text{T}A}\frac{(k_B T_{e,n})^{3/2}}{T_{p,n}^5} \quad , \tag{63}$$

where we have taken into account that $T_{e,n} \ll T_{p,n}$ in our case. If condition (63) is not valid, all cooling power is consumed by the electron-phonon heat flow in the junction area. Putting $\Delta = 200$ μeV, $\Sigma = 4{\cdot}10^9$ WK^{-5}m^{-3}, and $R_\text{T}A = 2{\cdot}10^{-10}$ Ωm^2 which is the smallest specific resistance of the junction with which we have observed cooling, and requiring that $T_{e,n} = 0.1$ K when $T_{p,n} = 0.3$ K, we get $d < 110$ nm. In practice d cannot be much above 30 nm if we want to get a significant cooling power for a sensor on a dielectric membrane.

The best lattice cooling result obtained is shown in Fig. 31. Contrary to the results obtained with the electron coolers, we have not been able to cool the lattice with the large junctions to $0.3T_\text{bath}$. The reason is excess volume of the normal metal on the bulk, which decreases the net cooling power. In the case of the cooler in question with $\Omega \approx 19$ $(\mu\text{m})^3$, the power transported from the electron system to the lattice is 22 pW. The maximum cooling power of the junctions with bath at 205 mK and electrons at 151 mK and a tunnel resistance of $R_T \approx 8$ Ω is from Eq. (61) 47 pW. The remaining ~ 20 pW is possibly lost due to the heating of the superconductor.

The importance of the result shown in Fig. 30 should not be underestimated: the fact that the trapping works well at the very lowest temperatures

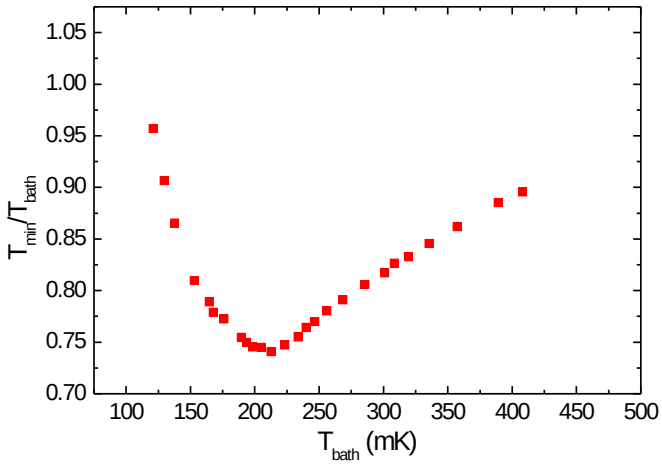

Figure 31: The best cooling result obtained with a lattice cooler with large area junctions. Thermometry of the isolated SiN membrane and the bulk Si was carried out with a pair of small SINIS junctions. The heating below 200 mK is due to the excessive heating of the superconductor due to non-perfect quasiparticle traps.

opens up the possibility for much larger junction areas with cooling power in the tens of nanowatts range.

7 Summary

The focus of this work has been the quest to pursue the sensitivity limits of thermal radiation detectors. Even though bolometric detection has some drawbacks, mainly the fact that it requires cooling to obtain competitive sensitivity, these detectors are unrivaled in terms of versatility and spectral range. These virtues make thermal detectors a rewarding field for an experimentalist such as myself to work in as there are so many applications where these devices can be used. What would the American astronomer Samuel P. Langley say if told that the device he used in 1901 to detect a cow across a field is nowadays used to detect nanokelvin variations in the Cosmic microwave background radiation!

In this thesis novel room temperature antenna-coupled microbolometers were developed in which a simple, robust surface micromachining technique was used to fabricate free standing titanium bridges. Although suffering from excessive $1/f$ noise, the results are encouraging and with some further materials study could reach NEPs in the 10 pW/$\sqrt{\text{Hz}}$ range at modulation frequencies below 1 kHz. There are immediate applications for these devices, two of which are the study of the millimetre-wave radiation from solar flare eruptions [64], and imaging of concealed weapons under clothing [65].

The superconducting Nb hot-spot bolometer developed within this thesis demonstrated a significant performance increase in terms of speed, NEP and dynamic range over existing 4.2 K bolometers. The possibility of constructing large integrated imaging arrays incorporating SQUID multiplexers opens one route to the realization of sensitive submillimetre-wave cameras for passive imaging applications in the field of security, medical imaging, and remote sensing. As single pixel devices, these detectors could benefit fast-scan submillimetre fourier transform spectrometry in which fast, broadband detectors are needed, and where the detectors used today require cooling to below 1 K in order to reach the NEP level we demonstrated at 4.2 K.

Although the transition-edge sensor microbolometers and microcalorimeters have been at the focus of a lot of attention in the recent years, we have shown that the picture hasn't yet been complete. The introduction of an additional source of noise has deepened our understanding of the transition-edge sensor, and this knowledge can be used in optimizing novel sensors. We feel that this study is important as a lot of effort is put to the development of hot-electron TES bolometers for the submillimetre-wave range [66, 67, 68]. Yet, the fluctuation superconductivity noise might not have as severe impact on these devices as the bias power they are operated at is much smaller than in the case of X-ray microcalorimeters.

In the end, the factor that will determine the prevalence of cryogenic de-

tectors is the efficiency, size, reliability and production cost of the cooling systems available. The ultimate goal is to have temperatures well below 1 K completely transparent to the end-user. One technology with such potential is the SINIS tunnel junction cooler, on which the the final part of this thesis was focused on. We showed that it is possible to increase the cooling power of SINIS coolers to the level that they are applicable for typical microcalorimeter dissipation levels. As the overheating of the superconducting electrode can be avoided with quasiparticle trapping, a natural continuation of this work would be the further increase of the junction size in conjunction with the use of novel substrate materials, such as porous silicon where the lattice heat transport is strongly suppressed. The physics have shown that the cooling method can be scaled to cooling stages, and the problems remaining are mostly technological.

References

[1] J. Zmuidzinas, "Progress in Coherent Detection Methods," in *The Physics and Chemistry of the Interstellar Medium, Proceedings of the 3rd Cologne-Zermatt Symposium, held in Zermatt, September 22-25, 1998* (V. Ossenkopf, J. Stutzki, and G. Winnewisser, eds.), (Herdecke), pp. 423–430, GCA-Verlag, Aug. 1999. ISBN 3-928973-95-9.

[2] H. Tananbaum, N. White, J. Bookbinder, F. Marshall, and F. Cordova, "Constellation X-ray mission: implementation concept and science overview," in *Proc. SPIE* (O. Siegmund and K. Flanagan, eds.), vol. 3765, (Bellingham, Washington 98227-0010 USA), pp. 62–72, SPIE, 1999.

[3] M. Bavdaz, J. Bleeker, G. Hasinger, H. Inoue, G. Palumbo, A. Peacock, A. Parmar, M. Turner, J. Truemper, and J. Schiemann, "X-ray evolving universe spectroscopy mission (XEUS)," in *Proc. SPIE* (R. Hoover and A. Walker, eds.), vol. 3766, (Bellingham, Washington 98227-0010 USA), pp. 82–93, SPIE, 1999.

[4] T. Passvogel and J.-J. Juillet, "Current status of the Herschel/Planck program," in *Proc. SPIE* (J. C. Mather, ed.), vol. 4850, (Bellingham, Washington 98227-0010 USA), pp. 598–605, SPIE, 2003. In press.

[5] A. Rogalski, "Infrared detectors: an overview," *Infrared physics & technology*, vol. 43, pp. 187–210, 2002.

[6] M. Fujiwara, "Development of far-infrared Ge:Ga photoconductor having a longitudinal configuration," *Appl. Phys. Lett.*, vol. 77, pp. 3099–3101, November 2000.

[7] R. Wood, *Monolithic Silicon Microbolometer Arrays*, vol. 47 of *Semiconductors and Semimetals*, ch. 3, pp. 43–122. San Diego: Academic Press, 1997.

[8] Infrared Labs InSb hot electron bolometer, http://www.irlabs.com.

[9] J. M. Gildemeister, A. T. Lee, and P. L. Richards, "A fully lithographed voltage-biased superconducting spiderweb bolometer," *Applied Physics Letters*, vol. 74, pp. 868–870, February 1999.

[10] L. Yujiri, H. Agravante, M. Biedenbender, G. Dow, M. Flannery, S. Fornaca, B. Hauss, R. Johnson, R. Kuroda, K. Jordan, P. Lee, D. Lo, B. Quon, A. Rowe, T. Samec, M. Shoucri, K. Yokoyama, and J. Yun,

[21] M. E. MacDonald, "Pattern and polarization measurements of integrated-circuit spiral antennas at 10 μm wavelength," in *Millimeter and Submillimeter Waves III* (M. N. Afsar, ed.), vol. 2842, (Bellingham, Washington 98227-0010 USA), pp. 501–512, SPIE, SPIE, 1996.

[22] A. Luukanen and V.-P. Viitanen, "Terahertz imaging system based on antenna-coupled microbolometers," *Proc. SPIE*, vol. 3378, pp. 34–44, April 1998.

[23] M. Kominami, D. Pozar, and D. Schaubert, "Dipole and slot elements and arrays on semi-infinite substrates," *IEEE Trans. Ant. Propag.*, vol. 33, pp. 600–607, Jun 1985.

[24] Sh. Kogan, *Electronic noise and fluctuations in solids*, ch. 8, pp. 227–229. Cambridge University Press, 1996.

[25] D. W. Floet, E. Miedema, and T. Klapwijk, "Hotspot mixing: A framework for heterodyne mixing in superconducting hot-electron bolometers," *Appl. Phys. Lett.*, vol. 74, no. 3, pp. 433–435, 1999.

[26] H. F. Merkel, P. Khosropanah, S. Cherednichenko, K. Yngvesson, A. Adam, and E. L. Kollberg, "A two-dimensional hot-spot mixer model for phonon-cooled hot electron bolometers," *IEEE Trans. Appl. Supercond.*, vol. 11, pp. 179–182, March 2001.

[27] R. Berman, *Thermal conduction in solids*, ch. 12, pp. 164–168. Oxford: Oxford University Press, 1976.

[28] Conductus iMAG LTS SQUID system.

[29] F. Pobell, *Matter and methods at low temperatures*. Berlin and New York: Springer-Verlag, 2nd ed., 1996.

[30] K. D. Irwin, G. C. Hilton, D. A. Wollman, and J. M. Martinis, "Thermal-response time of superconducting transition-edge microcalorimeters," *J. Appl. Phys.*, vol. 83, pp. 3978–3985, April 1998.

[31] M. Kiviranta, H. Seppä, J. van der Kuur, and P. Korte, "Squid-based readout schemes for microcalorimeter arrays," in *Low Temperature Detectors 9 (LTD-9)* (F. S. Porter, D. McCammon, M. Galeazzi, and C. Stahle, eds.), vol. 605 of *AIP Conference Proceedings*, (Melville, New York), pp. 295–300, American Institute of Physics, 2002.

[32] J. Chervenak, K. Irwin, E. Grossman, J. M. Martinis, and C. Reintsema, "Superconducting multiplexer for arrays of transition edge sensors," *Appl. Phys. Lett.*, vol. 74, pp. 4043–4045, Jun 1999.

[33] J. A. Hulbert and G. O. Jones, "The Superconducting Bolometer as a Detector of Thermal Radiation from Low-Temperature Sources ," *Proc. Phys. Soc. B*, vol. 68, pp. 801–804, Nov. 1955.

[34] J. Clarke, G. Hoffer, P. Richards, and N.-H. Yeh, "Superconductive bolometers for submillimeter wavelengths," *J. Appl. Phys.*, vol. 48, pp. 4865–4879, December 1977.

[35] J. Clarke, P. L. Richards, and N.-H. Yeh, "Composite superconducting transition edge bolometer," *Appl. Phys. Lett.*, vol. 30, pp. 664–666, June 1977.

[36] K. D. Irwin, "An application of electrothermal feedback for high resolution cryogenic particle detection," *Appl. Phys. Lett.*, vol. 66, pp. 1998–2000, April 1995.

[37] P. Blaha, K. Schwarz, and P. Dederichs, "Electronic structure of hcp metals," *Phys. Rev. B.*, vol. 38, pp. 9368–9374, nov 1988.

[38] C. Bean, "Magnetization of hard superconductors," *Phys. Rev. Lett.*, vol. 8, pp. 250–253, Mar 1962.

[39] E. Zeldov, J. R. Clem, M. McElfresh, and M. Darwin, "Magnetization and transport currents in thin superconducting films," *Phys. Rev. B*, vol. 49, pp. 9802–9822, Apr 1994.

[40] A. Luukanen, H. Sipilä, K.Kinnunen, A.Nuottajärvi, P.Hiltula, I.Suni, and J.P.Pekola, "Final report: Hot-electron microbolometers for far-infrared and submillimetrewave application." European Space Agency, ESA Contract 12835/98/NL/SB, December 2000. ESA-ESTEC, ADM-A, Keplerlaan 1, NL-2200 AG Noordwijk.

[41] A. T. Lee, P. L. Richards, S. W. Nam, B. Cabrera, and K. D. Irwin, "A superconducting bolometer with strong elecrothermal feedback," *Appl. Phys. Lett.*, vol. 69, pp. 1801–1803, September 1996.

[42] G. C. Hilton, J. M. Martinis, K. D. Irwin, N. F. Bergren, D. A. Wollman, and S. Nam, "Microfabricated transition-edge x-ray detectors," *IEEE Trans. Appl. Supercond.*, vol. 11, pp. 739–742, March 2001.

[43] O. Corbino, "Azioni elettromagnetiche doyute agli ioni dei metalli deviati dalla traiettoria normale per effetto di un campo," *Nuovo Cimento*, vol. 1, p. 397, 1911.

[44] M. Leivo and J. Pekola, "Thermal characteristics of silicon nitride membranes at sub-kelvin temperatures," *Appl. Phys. Lett.*, vol. 72, pp. 1305–1307, Mar 1998.

[45] H. Hoevers, "Transition edge sensors for imaging spectrometers," in *Low Temperature Detectors 9 (LTD-9)* (F. S. Porter, D. McCammon, M. Galeazzi, and C. Stahle, eds.), vol. 605 of *AIP Conference Proceedings*, (Melville, New York), American Institute of Physics, 2002.

[46] W. Bergmann Tiest, H. Hoevers, W. Mels, M. Ridder, M. Bruijn, P. Korte, and M. Huber, "Performance of x-ray microcalorimeters with an energy resolution below 4.5 eV and 100 μs response time," in *Low Temperature Detectors 9 (LTD-9)* (F. S. Porter, D. McCammon, M. Galeazzi, and C. Stahle, eds.), vol. 605 of *AIP Conference Proceedings*, (Melville, New York), pp. 199–202, American Institute of Physics, 2002.

[47] M. Lindeman, R. Brekosky, E. Figueroa-Feliciano, F. Finkbeiner, C. S. M. Li, C. Stahle, and N. Tralshawala, "Performance of Mo/Au tes microcalorimeters," in *Low Temperature Detectors 9 LTD-9* (F. S. Porter, D. McCammon, M. Galeazzi, and C. Stahle, eds.), vol. 605 of *AIP Conference Proceedings*, (Melville, New York), pp. 203–206, American Institute of Physics, 2002.

[48] R. Fujimoto, K. Mitsuda, N. Iyomoto, M. Audley, T. Miyazaki, T. Oshima, M. Yamazaki, K. Futamoto, Y. Takei, Y. Ishisaki, T. Kagei, T. Hiroike, U. Morita, T. Ohashi, N. Yamasaki, A. Kushino, H. Kudo, H. Sato, T. Nakamura, E. Goto, S. Shoji, T. Homma, T. Osaka, Y. Kuroda, M. Onishi, M. Goto, K. Tanaka, T. Morooka, S. Nakayama, and K. Chinone, "Status of X-ray microcalorimeter development at ISAS," in *Low Temperature Detectors 9 (LTD-9)* (F. S. Porter, D. McCammon, M. Galeazzi, and C. Stahle, eds.), vol. 605 of *AIP Conference Proceedings*, (Melville, New York), pp. 231–234, American Institute of Physics, 2002.

[49] Y. Ishisaki, U. Morita, T. Koga, K. Sato, T. Ohashi, K. Mitsuda, N. Yamasaki, R. Fujimoto, N. Iyomoto, T. Oshima, K. Futamoto, Y. Takei, T. Ichitsubo, T. Fujimori, S. Shoji, H. Kudo, T. Nakamura, T. Arakawa, T. Osaka, T. Homma, H. Sato, H. Kobayashi, K. Mori, K. Tanaka, T. Morooka, S. Nakayama, K. Chinone, Y. Kuroda, M. Onishi, and

K. Otake, "Present performance of a single pixel Ti/Au bilayer TES calorimeter," in *Proc. SPIE*, vol. 4851, (Bellingham, Washington 98227-0010 USA), SPIE, 2002. In press.

[50] P. Korte, W. Bergmann-Tiest, M. Bruijn, H. Hoevers, J. van der Kuur, W. Mels, and M. Ridder, "Noise and energy resolution of x-ray microcalorimeters," *IEEE Trans. Appl. Superc.*, vol. 11, pp. 747–750, mar 2001.

[51] M. K. Maul, M. W. Strandberg, and R. L. Kyhl, "Excess Noise in Superconducting Bolometers," *Phys. Rev.*, vol. 182, pp. 522–525, June 1969.

[52] L. Aslamasov and A. Larkin, "The influence of fluctuation pairing of electrons on the conductivity of normal metal," *Phys. Lett.*, vol. 26A, pp. 238–239, February 1968.

[53] R. Glover, "Ideal resistive transition of a superconductor," *Phys. Lett. A*, vol. 25, pp. 542–544, Oct 1967.

[54] K. Nagaev, "Theory of excess noise in superconductors above T_c," *Physica C*, vol. 184, pp. 149–158, 1991.

[55] M. Tinkham, *Introduction to superconductivity*, ch. 8, pp. 296–315. Singapore: McGraw-Hill, 1996.

[56] N. Kopnin. Private communication, 2002.

[57] D. M. S.H. Moseley, J.C. Mather, "Thermal detectors as x-ray spectrometers," *J. Appl. Phys.*, vol. 56, pp. 1257–1262, September 1984.

[58] M. Nahum, T. M. Eiles, and J. M. Martinis, "Electronic microrefrigerator based on a normal-insulator-superconductor tunnel junction," *Appl. Phys. Lett*, vol. 65, pp. 3123–3125, December 1994.

[59] M. M. Leivo, J. P. Pekola, and D. V. Averin, "Efficient peltier refrigeration by a pair of normal metal/insulator/superconductor junctions," *Appl. Phys. Lett*, vol. 68, pp. 1996–1998, April 1996.

[60] M. Leivo, A. Manninen, and J. Pekola, "Microrefrigeration by normal-metal/insulator/superconductor tunnel junctions," *Appl. Superc.*, vol. 5, pp. 227–233, 1998.

[61] P. A. Fisher, J. N. Ullom, and M. Nahum, "High-power on-chip microrefrigerator based on a normal-metal/insulator/superconductor tunnel junction," *Applied Physics Letters*, vol. 74, pp. 2705–2707, May 1999.

[62] J. P. Pekola, D. V. Anghel, T. I. Suppula, J. K. Suoknuuti, A. J. Manninen, and M. Manninen, "Trapping of quasiparticles of a nonequilibrium superconductor," *Appl. Phys. Lett.*, vol. 76, pp. 2782–2784, May 2000.

[63] S. R. Golwala, J. Jochum, and B. Sadoulet, "Noise considerations in low resistance NIS junctions," in *Proc. 7th Int. Workshop on Low Temperature Detectors LTD-7* (S. Cooper, ed.), (Munich, Germany), pp. 64–65, MPI Physik, July 1997.

[64] V. Khaikin, S. Yakovlev, A. Kazarinov, I. E. anf A. Volkov, and E. Valtaoja, "Multi-beam solar radio telescope of tuorla observatory: test operations.," in *URSI/IEEE XXVII Convention on Radio Science* (S. Tretyakov and J. Säily, eds.), (Espoo, Finland), pp. 84–87, Helsinki University of Technology, 2002.

[65] E. Grossman, A. Bhupathiraju, A. Miller, and C. Reintsema, "Concealed weapons detection using an uncooled millimeter-wave microbolometer system," in *Infrared and passive millimeter-wave imaging systems: Design, analysis, modeling and testing* (R. Appleby, G. Holst, and D. Wikner, eds.), vol. 4719, (Bellingham, Washington 98227-0010 USA), pp. 364–369, SPIE, SPIE, 2002.

[66] A. Sergeev, V. Mitin, and B. Karasik, "Ultrasensitive hot-electron kinetic-inductance detectors operating well below the superconducting transition," *Appl. Phys. Lett.*, vol. 80, pp. 817–819, Feb 2002.

[67] A. Goldin, J. Bock, C. Hunt, A. Lange, H. LeDuc, A. Vayonakis, and J. Zmuidzinas, "Samba: Superconducting antenna-coupled multi-frequency, bolometric array," in *Low Temperature Detectors 9 (LTD-9)* (F. S. Porter, D. McCammon, M. Galeazzi, and C. Stahle, eds.), vol. 605 of *AIP Conference Proceedings*, (Melville, New York), pp. 251–254, American Institute of Physics, 2002.

[68] M. J. Myers, A. Lee, P. Richards, D. Schwan, J. Skidmore, A. Smith, H. Spieler, and J. Yoon, "Antenna-coupled arrays of voltage-biased superconducting bolometers," in *Low Temperature Detectors 9 (LTD-9)* (F. S. Porter, D. McCammon, M. Galeazzi, and C. Stahle, eds.), vol. 605 of *AIP Conference Proceedings*, (Melville, New York), pp. 247–250, American Institute of Physics, 202.

"Passive millimeter-wave camera," in *Passive Millimeter-Wave Imaging Technology* (R. M. Smith, ed.), vol. 3064, (Bellingham, Washington 98227-0010 USA), pp. 15–22, SPIE, SPIE, 1997.

[11] P. Kangaslahti, T. Gaier, D. Dawson, J. Tuovinen, T. Karttaavi, M. Lahdes, N. Hughes, T. Cong, P. Jukkala, P. Sjöman, and S. Weinreb, "Low noise amplifiers in InP technology for pseudo correlating millimeter wave radiometer," *IEEE Microwave Symposium Digest, MTT-S*, vol. 3, pp. 1959–1962, 2001.

[12] P. H. Siegel, "Terahertz technology," *IEEE Trans. Microwave Theory Tech.*, vol. 50, pp. 910–928, Mar 2002.

[13] A. Semenov, H.-W. Hübers, H. Richter, M. Birk, M. Krocka, U. Mair, K. Smirnov, G. N. Gol'tsman, and B. M. Voronov, "2.5 THz heterodyne receiver with NbN hot-electron-bolometer mixer," *Physica C*, vol. 372-376, pp. 448–453, 2002.

[14] G. Goltsman, "Hot electron bolometric mixers: new terahertz technology," *Infrared Physics & Technology*, vol. 40, pp. 199–206, 1999.

[15] J. C. Mather, "Bolometer noise: non-equilibrium theory," *Appl. Opt.*, vol. 21, pp. 1125–1129, March 1982.

[16] R. C. Jones, "The general theory of bolometer performance," *J. Opt. Soc. Am.*, vol. 43, no. 1, pp. 1–14, 1953.

[17] H. Hoevers, A. Bento, M. Bruijn, L. Gottardi, M. Korevaar, W. Mels, and P. Korte, "Thermal fluctuation noise in a voltage biased superconducting transition edge thermometer," *Appl. Phys. Lett.*, vol. 77, December 2000.

[18] J. M. Gildemeister, A. T. Lee, and P. L. Richards, "Model for excess noise in voltage-biased superconducting bolometers," *Appl. Opt.*, vol. 40, pp. 6229–6235, December 2001.

[19] M. E. MacDonald and E. N. Grossman, "Niobium microbolometers for far-infrared detection," *IEEE Trans. Microwave Theory Tech.*, vol. 43, pp. 893–896, April 1995.

[20] E. N. Grossman, J. E. Sauvageau, and D. G. McDonald, "Lithographic spiral antennas at short wavelengths," *Appl. Phys. Lett.*, vol. 59, pp. 3225–3227, December 1991.

Abstracts of publications I–VI

I. In an European Space Agency funded research project, our goal is to develop microbolometer technology for x-ray and far-infrared detection for ESA's future scientific missions. We report results on the x-ray calorimeter, which is based on the superconducting transition of the Ti/Au thermometer strip at about 200 mK. Incident x-rays heat up a Bi absorber, deposited on top of the 400 μm $\times$ 400 μm thermometer. The temperature rise of the absorber is measured as a change of the thermometer current with a SQUID operating at 1 K.

II. Evaporation of hot electrons from a normal-metal into a superconductor can be used for efficient Peltier type cooling in micrometer size tunnel junctions. We have cooled the electrons to one third, and, as the main result of the present paper, a separate silicon nitride membrane to about one half of its starting temperature; all results have been obtained at temperatures well below 1 K, where the lattice is weakly coupled to electrons thermally. The micromachined membrane can serve as a thermal bath for tiny samples, like bolometric radiation detectors in astronomy.

III. Astronomical observations of cosmic sources in the far-infrared and X-ray bands require extreme sensitivity. The most sensitive detectors are cryogenic bolometers and calorimeters operating typically at about 100 mK. The last stage of cooling (from 300 mK to 100 mK) often poses significant difficulties in space-borne experiments, both in system complexity and reliability. We address the possibility of using refrigeration based on normal metal/insulator/superconductor (NIS) tunnel junctions as the last stage cooler for cryogenic thermal detectors. We compare two possible schemes: the direct cooling of the electron gas of the detector with the aid of NIS tunnel junctions and the indirect cooling method, when the detector lattice is cooled by the refrigerating system, while the electron gas temperature is decreased by electron-phonon interaction. The latter method is found to allow at least an order of magnitude improvement in detector noise equivalent power, when compared to the direct electron cooling.

IV. In this paper we report recent results obtained with large area superconductor-insulator-normal metal-insulator-superconductor tunnel junction coolers. With the devices we have successfully demonstrated electronic cooling from 260 mK to 80 mK with a cooling power of 20 pW at 80 mK. At present, we are focusing on obtaining similar

performance in cooling cryogenic detectors. Additionally, we present recent results of successful operation of a metal-semiconductor structure with a Schottky barrier acting as the tunnel barrier and the possibility to use this kind of structures for on-chip cooling.

V. We report the electrical properties of an antenna-coupled niobium vacuum-bridge bolometer, operated at a temperature of 4.2 K, in which the thermal isolation is maximized by the vacuum gap between the bridge and the underlying silicon substrate. The device is voltage-biased, which results in a formation of a normal state region in the middle of the bridge. The device shows a current responsivity of -1430 A/W and an amplifier limited electrical noise equivalent power of 1.4×10^{-14} W/$\sqrt{\text{Hz}}$.

VI. In order to investigate the origin of the until now unaccounted excess noise and to minimize the uncontrollable phenomena at the transition in X-ray microcalorimeters we have developed superconducting transition-edge sensors into an edgeless geometry, the so-called Corbino disk (CorTES), with superconducting contacts in the centre and at the outer perimeter. The measured rms current noise and its spectral density can be modeled as resistance noise resulting from fluctuations near the equilibrium superconductor-normal metal boundary.